

chapter seventeen

Ultrasonic additive manufacturing

Paul J. Wolcott and Marcelo J. Dapino

Contents

17.1	Introduction	275
17.1.1	UAM microstructure	279
17.2	Example builds and components.....	280
17.3	UAM process property relationships in aluminum alloys.....	288
17.3.1	Process parameter optimization	288
17.3.2	Process improvements studies	292
17.3.2.1	Foil overlap and stacking	292
17.3.2.2	Effects of surface roughness	294
17.3.2.3	Effect of heat treatments.....	296
17.3.3	Elastic modulus	298
17.4	Dissimilar material joining in UAM	300
17.4.1	Al/Ti dissimilar welding	300
17.4.2	Steel/Ta joining	303
17.4.3	Other dissimilar joining.....	305
17.5	Challenges and future directions.....	307
	References.....	311

17.1 Introduction

Worldwide sales of additive manufacturing products and services are estimated to reach \$11 billion in 2021, up from \$2 billion in 2012 [1]. Despite this anticipated level of growth, the value of additive manufacturing to industries that rely on mass manufacturing is unclear. As a relatively new technology, additive manufacturing has not yet reached the levels of throughput, cost effectiveness, and standardization required for implementation in industry sectors such as automotive and electronics. Ultrasonic additive manufacturing (UAM), a niche technology within the additive manufacturing area, offers the manufacturing industry a different approach for creating lightweight metal-based structures incorporating dissimilar metals, nonmetallic materials, smart materials, and intricate features that are difficult to produce through conventional means. In-depth research is needed to address the challenges posed by this relatively new technology and to move UAM from the laboratory to practical applications. This chapter discusses those challenges and presents research efforts conducted by the authors and other researchers to understand the process.

UAM, a solid-state 3D-printing technology based on traditional ultrasonic metal welding, [2] makes it possible to fabricate metal structures from foil stock. The fundamental principle of UAM operation is the layering of foils through solid-state metal welding to

achieve fully dense, gapless 3D parts. In a broad sense, UAM can also be used as a joining technology to integrate dissimilar metals, seam welding of metallic sheets, [3] or as a cladding technology by which high-value materials are layered over a bulk substrate. UAM structures can also incorporate dissimilar metals along with embedded features such as reinforcement fibers, smart sensors and actuators, and heat-wicking materials. In addition, UAM has been shown to address various traditional joining and manufacturing needs such as joining of metals to nonmetals, provided suitable joint configurations are developed. [Figure 17.1](#) illustrates possible uses for UAM.

A key benefit of UAM as a technology for 3D printing of metals and joining of dissimilar materials is that process temperatures are low, typically less than one half of the melting temperature of aluminum alloys [4,5]. The low thermal loading inhibits the formation of brittle intermetallics with the subsequent advantage of not altering the microstructure of the constituent metals. Low operating temperatures also can limit corrosion through mitigation of electrochemical reactions. Further, finished parts suffer no heat-induced distortion, and hence no remedial machining is required to bring parts to their intended dimensions.

In the UAM process, a sonotrode driven by one or more piezoelectric transducers imparts ultrasonic vibrations to a metal foil, creating a scrubbing action and plastic deformation between the foil and the material to which it is being welded ([Figure 17.2a](#)). The vibration frequency is nominally 20 kHz on most systems.

The scrubbing action displaces surface oxides and contaminants and collapses asperities, exposing nascent surfaces that instantaneously form a metallurgical bond under a compressive force. The first layer is welded onto a metal baseplate, which is used to support the build. By welding a succession of tapes, first side by side and then one on top of one another, a three-dimensional metal part can be fabricated [2]. Periodic machining with a computer numerical control (CNC) stage ([Figure 17.2b](#)) or laser-etching system allows

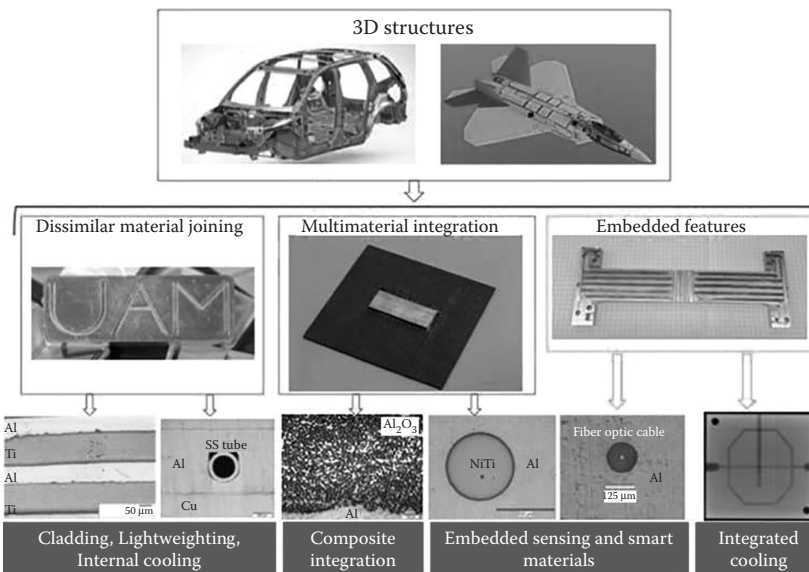


Figure 17.1 Potential UAM applications and capabilities. Low UAM process temperatures allow joining of dissimilar metals without the formation of brittle intermetallics and the integration of temperature-sensitive components, smart materials, cooling channels, organic polymers, and electronics into metal matrices.

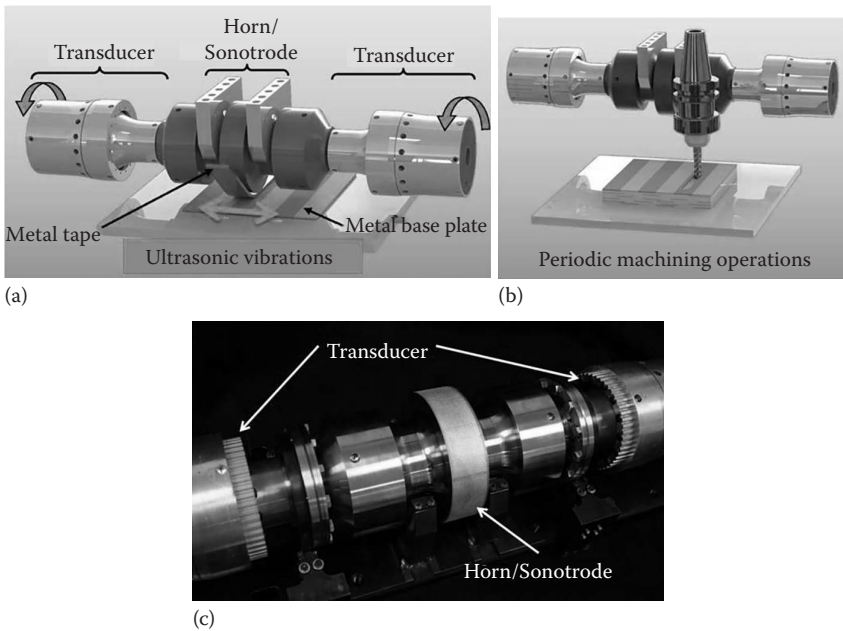


Figure 17.2 (a) Schematic of a UAM welder, which utilizes ultrasonic vibrations and pressure to join foil stock to a baseplate or other foils. The process is solid state, implying that no melting is present; (b) the process usually features a CNC mill for conducting subtractive operations; and (c) image of a welder outside of the machine indicating the transducers and sonotrode. The welder is acoustically tuned, so that the sonotrode resonates at 20 kHz (nominal).

for selective material removal and *in situ* machining to final dimensions. Depending on the part being built, additive and subtractive processes are repeated in various sequences until a solid component has been created or material has been added to a component. The subtractive processes are also utilized to create internal channels for thermal management, to align fibers within the matrix, or for surface texturing of embedded fibers. Upon completion of the build, the baseplate and build can be separated by conventional or electrical discharge machining (EDM) if this material is not desired in the final design.

The most advanced UAM systems [6] deliver 9 kW of ultrasonic power to the weld interface, which improves the strength and quality of UAM builds, greatly enhances the ability to weld dissimilar materials, and enables the construction of previously unfeasible adaptive structures (Figure 17.3). This is illustrated in Figure 17.4, where the metallurgical section of an aluminum 3003 build using a 1 kW UAM system shows gaps, in contrast to a build made with a 9 kW UAM system which shows no gaps despite the material used being aluminum 6061. Even though a low-void content does not guarantee high mechanical strength, [7] obtaining gapless builds is a necessary condition for optimizing the strength of UAM components.

Fundamental investigations in the field of UAM are aimed at creating an exact understanding of the process and to develop experimental approaches and models to describe the relationship between process conditions and build properties. As with ultrasonic metal welding, the main control variables for the UAM process include weld speed (or time), down force (or pressure), and vibration amplitude [2,8]. Ultrasonic vibration frequency is fixed at the designed resonance frequency of the sonotrode. For some materials, a heat



Figure 17.3 (See color insert.) State of the art UAM system featuring a 9 kW welder and 20 kN of normal force. This amount of power makes it possible to make high quality, gapless metallic parts.

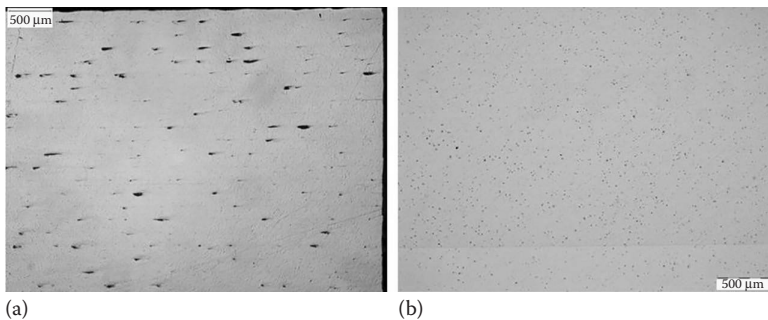


Figure 17.4 (a) Metallurgical section of aluminum 3003 build showing gaps left by 1 kW UAM system and (b) metallurgical section of gapless aluminum 6061 build fabricated with the 9 kW UAM system shown in [Figure 17.3](#).

plate is utilized to further intensify softening and enhance weldability. However, quality, void-free welds can be achieved for many aluminum alloys with no additional heating, as shown by way of example for Al 6061 [9].

UAM joining of relatively soft alloys including Al 3003 and Cu 1100 has been extensively studied [7–12]. These alloys are known to react well to the ultrasonic metal-welding process and have been shown to be compatible with the UAM process. More recent work performed on 9 kW systems has successfully demonstrated the fabrication of Al 6061 [9] builds and Al/Ti composites [13]. However, how harder materials such as iron alloys respond to the UAM process is not yet fully understood, in part due to current difficulties in fabricating iron-based UAM builds. Since these alloys do not deform easily, higher normal force and ultrasonic power are needed to achieve successful UAM joints. The increased mechanical rubbing, combined with an affinity to the steel sonotrode, leads to foils welding to the sonotrode, known as nuggets. This technological barrier may be addressed by

brazing certain ceramic materials to the sonotrode, reducing the affinity for bonding to the sonotrode, and therefore increasing the likelihood of generating viable welds.

17.1.1 UAM microstructure

The microstructure of UAM built structures has been extensively investigated using optical microscopy, scanning electron microscopy (SEM), focused ion beam (FIB), and transmission electron microscopy (TEM) techniques [11,14–16]. Such investigations have shown that within approximately 15 μm of the bond interface region, an area of small recrystallized grains exists [11,15,17]. Figure 17.5 shows an electron backscatter diffraction image of the bond interface in a UAM sample. Within the bond interface, small, mostly equiaxed grains are observed, whereas the bulk of the foils shows an elongated microstructure from the original rolling texture. Similarly, the polar mapping of the grain orientations shows a distinct texture in the bulk due to rolling, whereas the interface region is much more equiaxed. TEM measurements showing this effect have been presented by Johnson [14]. These observations indicate that a small recrystallized zone exists within approximately 15 μm of the bond interface, whereas the remainder of the bulk material has the same microstructure as the as-received foils.

The equiaxed grains at the bond interface indicate that a highly localized process of recrystallization has occurred due to deformation and limited heating during processing [10]. The equiaxed grain structure within the interface has a $111 \langle 110 \rangle$ shear texture [15]. A shear texture of this type is expected to have developed through the scrubbing action of the sonotrode and the deformation of microasperities at the interface of each material.

A bond theory of the UAM process is developed based on these findings, which is described as follows. The scrubbing action delivered to the bonding interfaces via the sonotrode creates plastic deformation, collapses asperities, removes surface oxides and contaminants from the faying surfaces, and creates nascent metal surfaces that instantaneously bond under sufficient normal force. Figure 17.6 illustrates this bond progression. In steps 1–3, microasperities are present or formed on the surface of the foil. Dynamic recrystallization occurs through the deformation and heating of this surface after sonotrode contact. During steps 4–6, an additional tape is being welded. During the weld process, dynamic recrystallization occurs by shear deformation of the microasperities on the material surfaces. Therefore in the interface region, a fine-equiaxed grain structure is formed in the microasperity locations. The interface region then expands by static recrystallization,

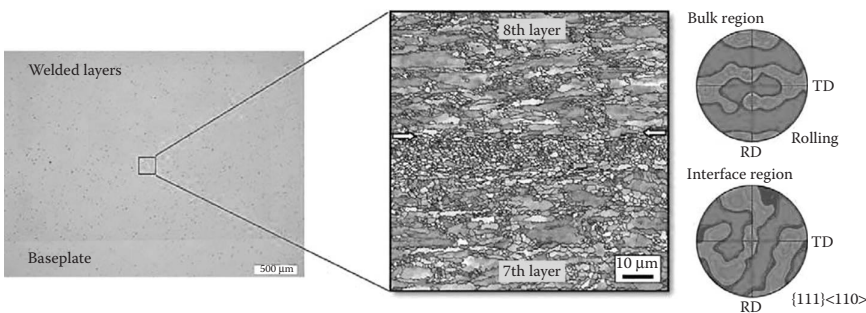


Figure 17.5 Electron backscatter diffraction (EBSD) image showing grain maps colored by inverse pole figure along with pole figure indicating strong rolling texture in bulk region and recrystallized texture in interface region. (From H. Fujii, M. Sriraman, and S. Babu, *Metallurgical and Materials Transactions A*, 42A, 4045–4055, 2011.)

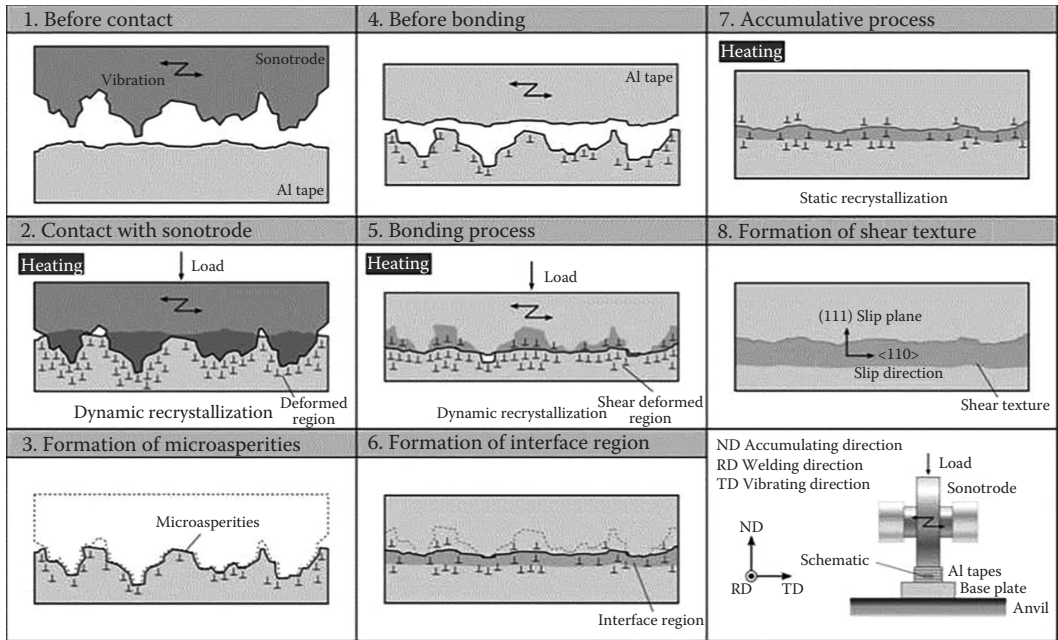


Figure 17.6 Schematic illustration of the microstructural evolution of the UAM process. Steps 1–3 show formation of microasperities due to plastic deformation of the top surface due to sonotrode contact, steps 4–6 show the bond formation process, and steps 7–8 show the effects of cumulative loading. (From H. Fujii, M. Sriraman, and S. Babu, *Metallurgical and Materials Transactions A*, **42A**, pp. 4045–4055, 2011.)

whereas additional tapes are subsequently welded, as shown in steps 7–8. Further, a shear texture is developed during this cumulative process which is oriented with the vibrating direction.

17.2 Example builds and components

Due to the low temperatures involved, the UAM process is a proven method for creating unique components including smart structures, thermal management devices, parts with embedded fibers, selectively reinforced parts, and dissimilar material joints. The temperatures of the UAM process are on the order of 150°C, well below the critical temperatures of smart materials, enabling incorporation into metallic structures without degradation of their properties as in fusion-based processes [5,17]. An example build incorporating Galfenol into aluminum is shown in [Figure 17.7](#). Galfenol, an alloy of iron and gallium, exhibits moderately high magnetostriction (magnetic field-induced strain) and magnetoelasticity, whereby the material changes its magnetization when stressed. These responses are used to design sensors and actuators with fast dynamic response, few to no moving parts, and compact operation. Galfenol withstands combined mechanical loads, tension, and shear, and it can be machined and formed using conventional means. When implemented into aluminum structures via UAM, the Galfenol element is shielded from outside factors and the resulting robust composites can be used as contact-less sensors, electrically tunable variable resonators, and solid-state actuators. [Figure 17.8a](#) and [b](#) shows model calculations for Galfenol composites, where the effect of Galfenol volume fraction on the normalized natural frequency is shown as a function of magnetic field. [Figure 17.8c](#)

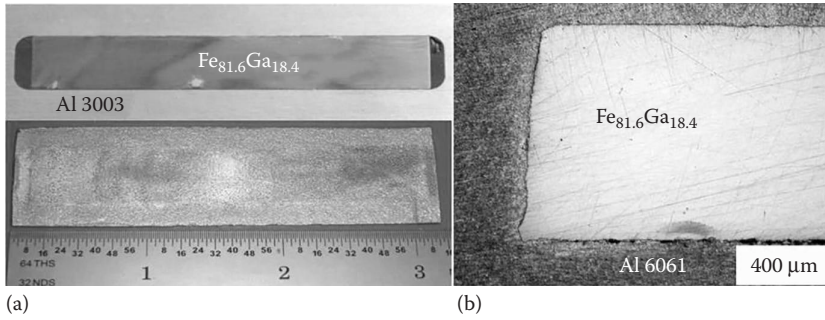


Figure 17.7 (a) Galfenol composite before and after UAM integration and (b) optical microscopy image of a Galfenol composite's cross section.

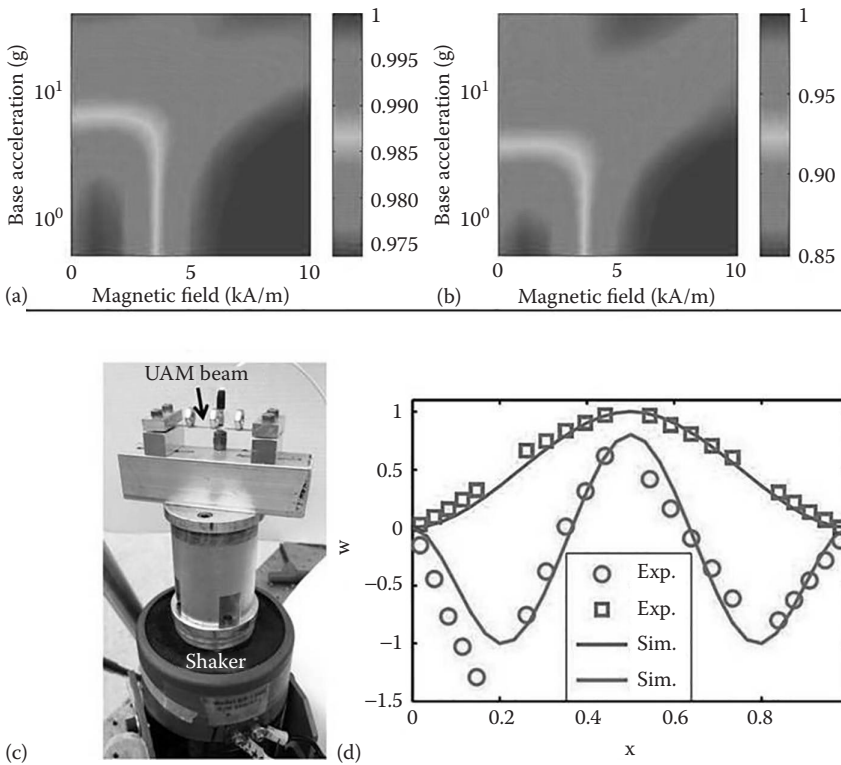


Figure 17.8 (a) Model results for normalized resonant frequency of the third bending mode at 10% Galfenol volume fraction, (b) 46% Galfenol volume fraction, (c) image of setup for testing Galfenol-aluminum beam, and (d) comparison of mode shapes from model and experimental results.

and d shows the test setup and performance of a Galfenol-aluminum composite under a mechanical load showing comparisons of experimental results with model simulations for the third bending mode. Testing was conducted using a mechanical shaker to induce specified vibration modes and measured with a laser vibrometer.

Another smart material system that can be integrated into metal matrix composites with UAM is Ni-Ti. Shape memory Ni-Ti, or Nitinol, exhibits large strains under thermal

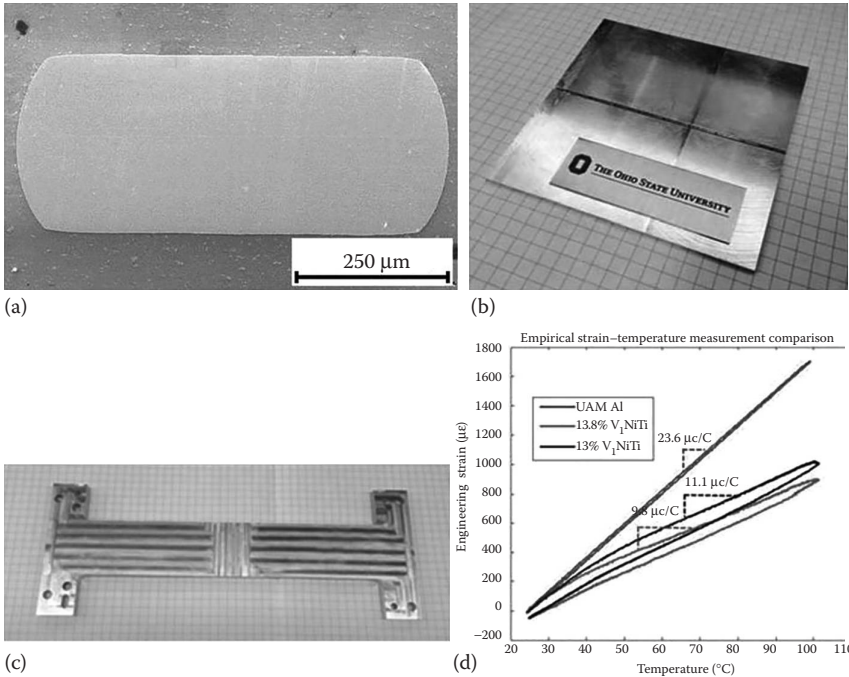


Figure 17.9 (a) Cross section of Ni-Ti wires embedded into Al 6061, (b) solid-state Ni-Ti hinge, (c) Ni-Ti beam for coefficient of thermal expansion mitigation, and (d) performance of Ni-Ti composite during thermal loading showing decreased thermal expansion with higher volume fraction.

loading due to a solid-state phase change to and from a memorized shape. The material is able to withstand very large elastic strains and actuate under thermal loads. These characteristics make Ni-Ti a suitable material for small, solid-state hinges and can also be used in the creation of composites with low coefficient of thermal expansion. Examples of Ni-Ti composites are shown in Figure 17.9. The cross section in Figure 17.9a shows the complete integration of a Ni-Ti ribbon into an aluminum matrix. A solid-state hinge is shown in Figure 17.9b, whereas the beam shown in Figure 17.9c is an aluminum and Ni-Ti composite which exhibits decreased thermal expansion when heated. Results of testing this composite are presented in Figure 17.9d showing the change in thermal expansion with Ni-Ti volume fraction. As the composite heats up, the aluminum matrix expands, whereas the Ni-Ti elements contract as they undergo a phase change from martensite to austenite, therefore leading to a net decrease in thermal expansion for the overall composite structure.

In addition to metallic smart materials, polymers and fiber optics can be integrated into composites using the UAM process. Figure 17.10 shows beta-phase polyvinylidene fluoride (PVDF), an active polymer with extremely high-frequency response and sensitivity, embedded in aluminum for purposes of integrated impact detection. When the surface of the aluminum plate is struck by an object, the stress that propagates through the structure creates a polarization change in the PVDF element that results in a voltage across thin electrodes deposited on the polymer. An insulating layer such as Kapton is used to prevent electrical conductivity between the electrodes and aluminum matrix. The frequency response of commercial PVDF embedded via UAM has been shown to be in the MHz range [18].

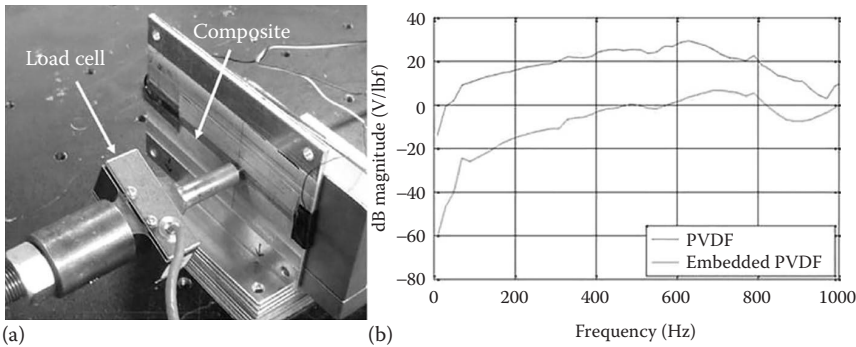


Figure 17.10 (a) Impact detection concept using PVDF embedded into aluminum using UAM and (b) response of PVDF sensor in air and embedded. The amplitude difference is caused by attenuation of the applied stress field due to damping in the host material.

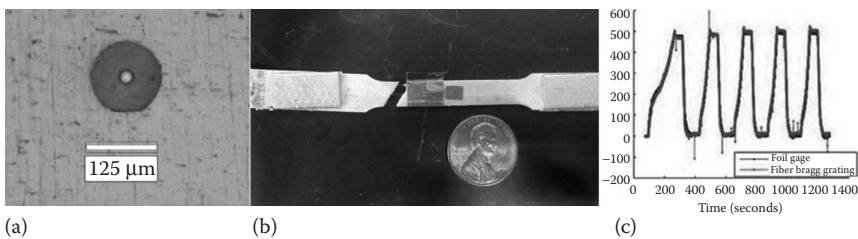


Figure 17.11 (a) Cross section of fiber optic wire embedded into Al 6061, (b) image of fiber Bragg grating embedded into aluminum and strain gage attached to surface, and (c) comparison of responses of fiber optic sensor and strain gage under a step load input.

Implementation of fiber optics into components can be done for *in situ* health monitoring without affecting the structural properties of the component being monitored. An example build with an embedded fiber optic sensor is shown in [Figure 17.11](#). The sensor is a fiber Bragg grating which detects very small displacements through frequency shifts in monochromatic light waves passing through the sensor. The fiber is completely encapsulated in the surrounding aluminum matrix without suffering degradation of mechanical or optical properties. Comparison of the sensor performance to a strain gage is shown in [Figure 17.11c](#). The two signals track extremely closer to one another, indicating the sensor is unaffected due to the integration into the aluminum matrix. Use of these types of devices can allow for longer part duration, as the component performance can be monitored throughout its lifetime.

State of the art UAM systems are built within a CNC machining framework, controlling table motion and maintaining the ability to perform machining operations. The ability to conduct welding and milling operations in tandem allows for creation of components with unique channel geometries built into the structure. An example device is shown in [Figure 17.12](#), in which channels traverse throughout the build. The image is an X-ray of the build showing the channels as darker areas on the image. UAM thus makes it possible to create unique thermal management devices with cooling channels that are difficult to achieve using other processes, in addition to dissimilar materials with suitable thermal properties.

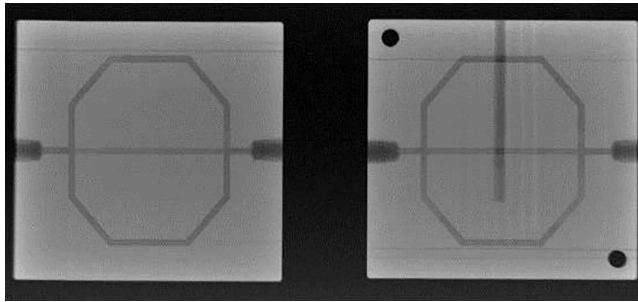


Figure 17.12 X-ray of UAM build with internal channels for thermal management.

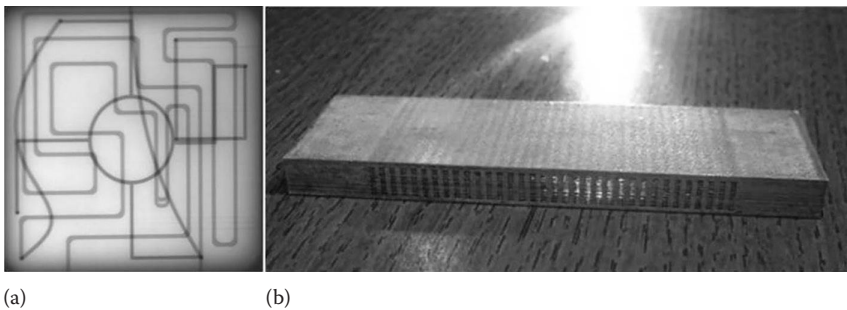
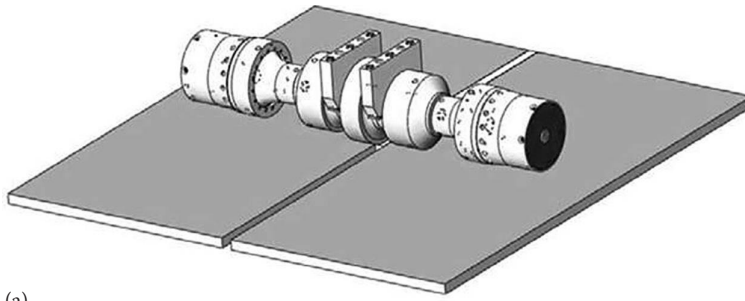


Figure 17.13 (a) X-ray of UAM component with a complex array of cooling channels in aluminum and (b) cross section of channels traversing an aluminum build. (Courtesy of Fabrisonic LLC.)

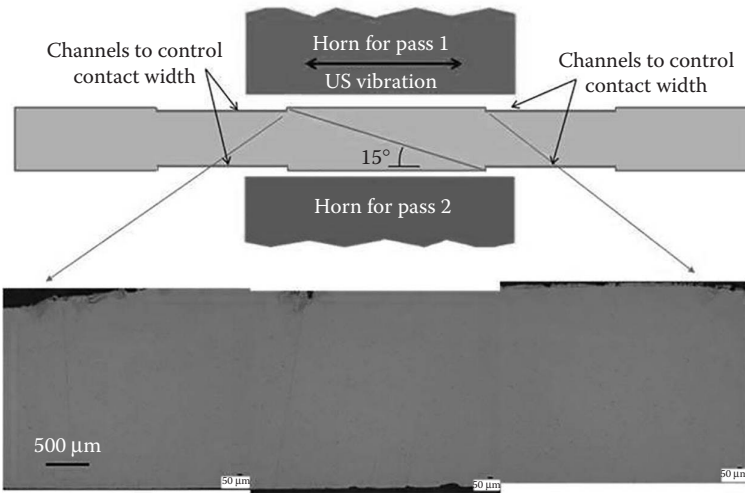
Additional examples of embedded features are shown in [Figure 17.13](#). [Figure 17.13a](#) shows an X-ray of a device with conformal cooling channels incorporated throughout the structure, whereas [Figure 17.13b](#) shows a part with many channels traversing through the aluminum structure. These types of components can be used for highly efficient, localized cooling in applications for power generation, electronics, manufacturing, and other industries.

The typical joint configuration in the UAM process uses thin foil, on the order of 0.005 in. thick, welded onto a baseplate or previous foil layers. However, recent developments have enabled the joining of aluminum sheet material 0.076 in. thick using a scarf joint geometry [3]. The concept uses UAM equipment to create a seam weld of two aluminum sheets, illustrated in [Figure 17.14a](#). By utilizing a scarf joint configuration and welding on both sides of the sheet, seamless joints can be achieved with properties similar to bulk material. A schematic of the configuration along with a cross section from a joint is shown in [Figure 17.14b](#), where no voids are apparent. This design effectively demonstrates that the UAM process can be used for joining of sheet material with properties matching bulk material, resulting in parts with no protrusions into flow fields exhibited by mechanical fasteners such as rivets. A key advantage of this approach over friction stir welding is the lower capital cost involved.

Similar to the concepts introduced with smart materials, passive materials can be incorporated into metal matrix structures as well. Passive fibers such as carbon fiber can be incorporated into aluminum utilizing the UAM process. Examples are shown in [Figure 17.15](#). In [Figure 17.15a](#), a carbon fiber composite is shown integrated with aluminum, while carbon nanopaper embedded into an aluminum matrix is shown in [Figure 17.15b](#).

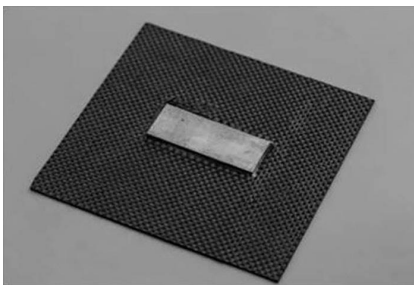


(a)

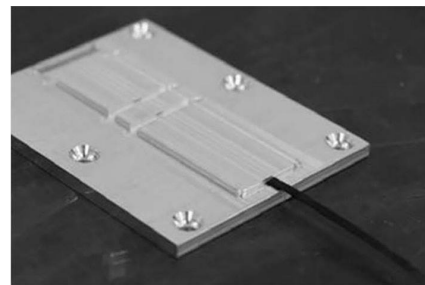


(b)

Figure 17.14 (a) UAM-based approach for butt joining sheet material and (b) schematic and cross section of a viable joint created using the process.



(a)



(b)

Figure 17.15 (a) Carbon fiber incorporated with aluminum build using UAM and (b) carbon nanopaper embedded into an aluminum matrix using the UAM process.

The integration of passive fibers or wires can be used for selective reinforcement. High stress areas of components can be reinforced, whereas areas of little to no load can remain thin for lightweighting purposes. One such material used for localized reinforcement is MetPreg, a metal matrix composite prepreg made of an aluminum matrix and continuous alumina ceramic fibers. This material can be readily welded using the UAM process, with examples shown in Figure 17.16.

Other examples of reinforcement include the incorporation of high-strength steels into an aluminum matrix. A cross section from a build with a stainless steel mesh embedded into aluminum is shown in Figure 17.17.

Similar to the MetPreg composites, this construct can allow for selective property control. Properties such as stiffness and strength can be controlled within a single component, allowing gradients of functionality where specific needs are required.

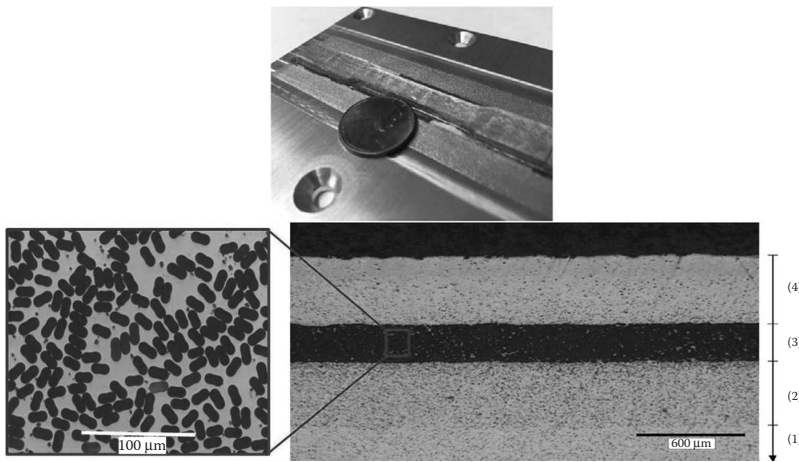


Figure 17.16 Image of MetPreg build in aluminum and cross section of a UAM build using MetPreg, a metal matrix composite prepreg. Sections on the macrosection are described as (1) baseplate material, (2) four layers of Al 6061 tape, (3) one layer of MetPreg, and (4) four layers of Al 6061 tape.

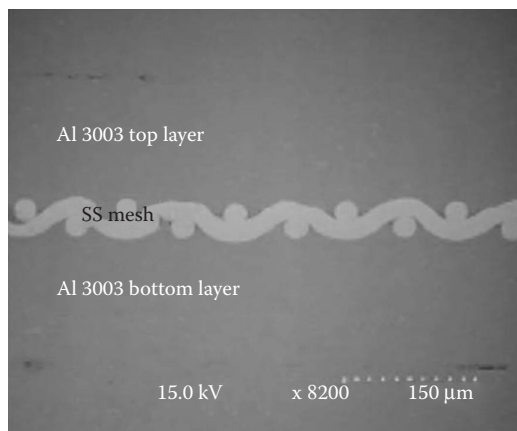


Figure 17.17 Cross section of UAM build with stainless steel mesh embedded for improved strength and stiffness. (From G.D. Janaki Ram, C. Robinson, Y. Yang, and B.E. Stucker, *Rapid Prototyping Journal*, 13(4), 226–235, 2007.)

The UAM process is a proven method of creating dissimilar material joints. It was established before in this article that because the process operates at low temperatures compared to fusion-based methods, diffusion is inhibited, therefore preventing the formation of brittle intermetallic layers at the bond interface. This key property of the UAM process has motivated trials on new material combinations, demonstrating that numerous material combinations are possible and many more are expected to be viable. Example uses of dissimilar joints include lightweight armors, cladding of high-value materials onto standard materials, and materials with tailored properties. A laminate of aluminum and titanium is shown in Figure 17.18 for a ballistic armor application. This construct enables high ballistic resistance while reducing weight overall compared to thick steel armors.

An example of cladding is presented in Figure 17.19, where aluminum foils are welded onto a stainless steel substrate. These types of joints are of growing importance in the integration of lightweight aluminum components into larger substructures. Although aluminum and stainless steel are highlighted, many other combinations have been proven, including Al/Cu, Al/Zn, Cu/Ni, Al/Ag, Cu/Ag, Mo/Al, Ta/Al, and Ni/stainless steel [19–22].

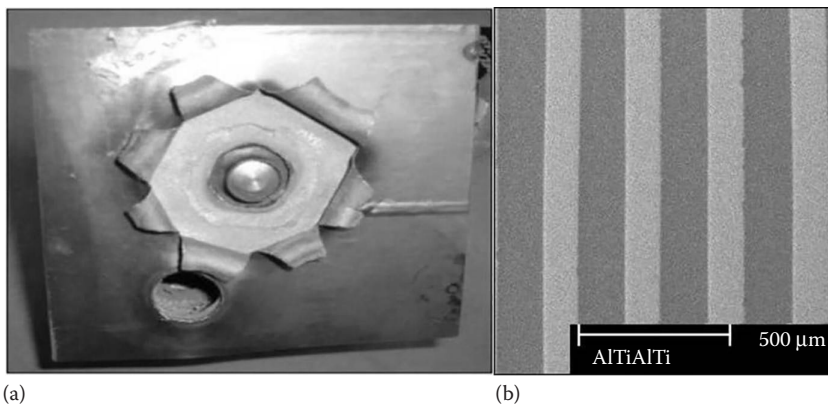


Figure 17.18 (a) Al-Ti laminate armor created using UAM and tested via ballistic impact and (b) cross section of Al-Ti laminate armor. (Courtesy of Fabrisonic LLC.)

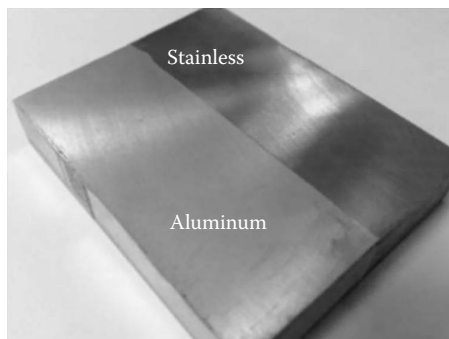


Figure 17.19 Image of aluminum foils welded onto a stainless steel substrate. (Courtesy of Fabrisonic LLC.)

17.3 UAM process property relationships in aluminum alloys

17.3.1 Process parameter optimization

Process parameters that are commonly controlled to affect the build quality of the UAM process are weld force, weld speed, weld amplitude, and baseplate temperature. These parameters must be optimized in order to create components with maximum build strength. In order to determine optimal process parameters, a study was performed joining Al 6061-H18 foil using the 9 kW UAM process [9]. A design of experiments (DOE) approach was used such that multiple processing parameters could be explored simultaneously. The study uses fully work-hardened Al 6061 which was purchased in the annealed heat treatment and fully work-hardened cold working condition, known hereafter as Al 6061-H18. Al 6061 was chosen due to its frequent use in industry and strong compatibility with UAM. Samples were manufactured on a Fabrisonic SonicLayer 4000 9 kW UAM machine. The machine is fully automated and includes CNC and laser-machining capabilities to complement the additive ultrasonic welding stage.

The DOE approach determines the optimal process parameters through mechanical strength testing of multiple build strips manufactured with varying process parameters. Build strips were generated for the DOE following a Taguchi L18 design matrix by varying the temperature, weld force, weld amplitude, and weld rate. The design matrix is shown in Table 17.1 with the 1, 2, and 3 designations indicating the low, medium, and high levels, respectively, for each of the parameters within a treatment combination. This type of experimental design allows for investigation of the effect that each parameter has on mechanical strength in a minimal number of experimental runs. The exact levels for each

Table 17.1 Taguchi L18 orthogonal array including 18 treatment combinations and three levels (low, medium, and high) for each of the four parameters investigated: temperature, weld force, weld amplitude, and weld rate

Treatment combination	Temperature	Weld force	Amplitude	Weld rate
1	1	1	1	1
2	1	1	2	2
3	1	1	3	3
4	1	2	1	1
5	1	2	2	2
6	1	2	3	3
7	1	3	1	2
8	1	3	2	3
9	1	3	3	1
10	2	1	1	3
11	2	1	2	1
12	2	1	3	2
13	2	2	1	2
14	2	2	2	3
15	2	2	3	1
16	2	3	1	3
17	2	3	2	1
18	2	3	3	2

of the parameters were determined from a pilot study, which established the build envelope of parameter levels for the study. These parameters are given in Table 17.2. The lower limit signifies levels of parameters where welds could not occur, whereas the upper limit indicates when the foils would weld to the sonotrode as opposed to the previous layer. This DOE methodology has been applied to the UAM process to determine optimal process parameters in 1 kW UAM for Al 3003, titanium to Al 3003, and stainless steel alloys, proving an effective method of determining the best process parameters for mechanical strength [7,19,23].

Weld strips were built following the Taguchi matrix on four baseplates, with nine strips welded onto each plate in 15/16 in. (23.81 mm) wide strips. Temperature was held constant during welding at either room temperature or 200°F, whereas the location on the plate was randomized for each parameter set. Push-pin tests were conducted after the samples were built. Further details on push-pin testing were provided by Zhang et al. [24]; subsequent studies in which this type of testing was directly applied to UAM include, for instance, Truog [25]. For the tests, 20 layers were welded onto a 12.7 mm (0.5 in.) thick baseplate with the weld strips built such that four test specimens could be machined from each strip. An example baseplate with UAM welds is shown in Figure 17.20. Utilization of solid baseplate material in the sample designs reduced the required number of layers, thus expediting the testing. Push-pin testing was conducted using a Gleeble thermal–mechanical system, where a pin was pressed into the sample while load and displacement of the frame were recorded.

Results from a representative push-pin treatment combination for a good bond are shown in Figure 17.21. A poor bond implies that the failure is predominately driven by delamination between layers, whereas a good bond implies that the failure is predominately driven by tensile failure of the layers. In the latter case, the pin presses through the layers forcing a failure which propagates through the foils, rather than by delamination.

Following mechanical testing, an analysis of variance (ANOVA) was performed on the measured data. The ANOVA is used to examine three or more variables, in this case the four parameters listed in Table 17.2, for statistical significance within a process. Main effects' plots are then used to indicate the optimal levels of the parameters for mechanical strength. The ANOVA uses a generalized linear model with four main effects, with the model equation given by

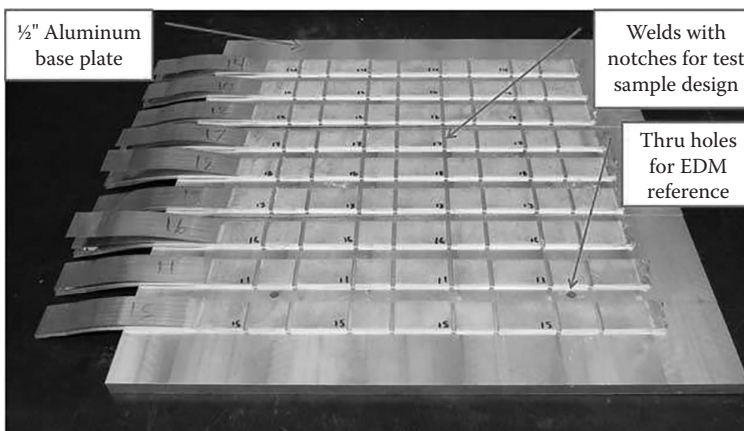


Figure 17.20 Test strips from push-pin sample manufacturing.

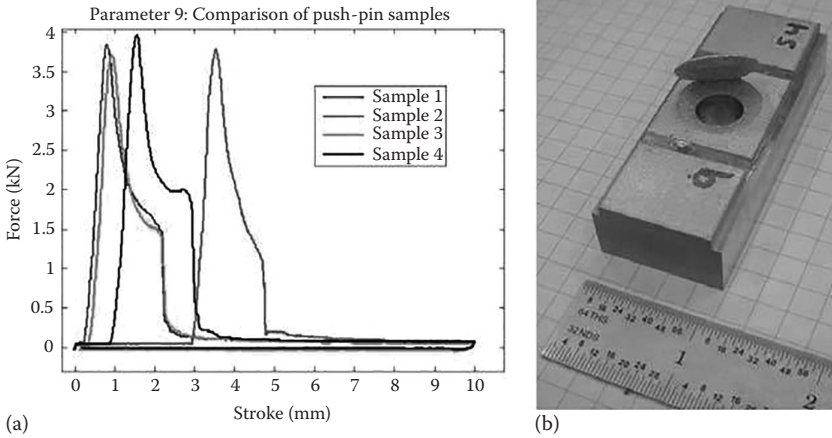


Figure 17.21 (a) Push-pin results for parameter set 9 representing good interlaminar failure and (b) sample built with parameter set 9.

Table 17.2 Parameter levels for each of the DOE treatment combinations

Parameter	Level 1	Level 2	Level 3
Temperature	22.2°C (72°F)	93.3°C (200°F)	–
Force	4000 N	5000 N	6000 N
Amplitude	28.28 μm	30.47 μm	32.76 μm
Speed	84.6 mm/sec (200 in./min)	95.2 mm/sec (225 in./min)	105.8 mm/sec (250 in./min)

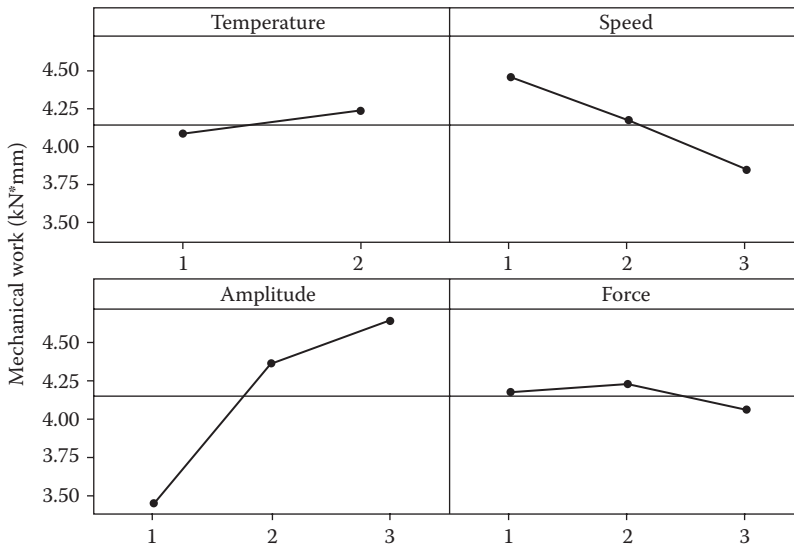
$$Y_{ijklt} = \mu + \alpha_i + \beta_j + \gamma_k + \delta_l + \epsilon_{ijklt} \tag{17.1}$$

This linear equation models the dependence of the response variable, Y_{ijklt} , on the levels of the treatment factors [26]. In Equation 17.1, μ is the overall average of the response variable (in this case, push-pin strength), and α_i , β_j , γ_k , and δ_l represent the effects of each of the process parameters on the mean response. In this case, α_i is the effect of temperature at the i th level on the response, while the other factors are fixed. Similarly, β_j , γ_k , and δ_l represent the effects of weld force, amplitude, and weld rate at the j th, k th, and l th levels, respectively, while the other factors are fixed. The error variable, ϵ_{ijklt} , is a random variable with normal distribution and zero mean, which denotes any variation in the response unaccounted for by the main four process parameters.

ANOVA results are given in Table 17.3 using the area under the force-displacement curve representing mechanical work as the response variable. In a statistical analysis, the p value represents the probability of obtaining a test at least as extreme as the one observed, assuming that the null hypothesis of no trend or no effect is true; p values less than 0.05 were chosen to indicate that a particular source of variation is statistically significant in the process. This means that a source of variation has a 95% likelihood of being a statistically significant influence on the process. In this case, amplitude and speed are considered significant with p values lesser than 0.001 and 0.007, respectively. Both temperature and force have p values greater than 0.05 and are therefore considered statistically insignificant.

Table 17.3 ANOVA results for push-pin testing using mechanical work as the response variable

Source	DF	Adj SS	Adj MS	F-ratio	p-value
Temperature	1	0.4018	0.4018	0.94	0.337
Weld force	2	0.3689	0.1845	0.43	0.652
Amplitude	2	19.1955	9.5977	22.39	<0.001
Weld speed	2	4.5869	2.2934	5.35	0.007
Error	64	27.4299	0.4286	–	–
Total	71	51.9830	–	–	–

**Figure 17.22** Main effects plot of push-pin test for each factor.

Main effects' plots shown in [Figure 17.22](#) visually confirm the ANOVA results. The amplitude plot shows a significant increase in mechanical work with increasing amplitude, whereas the mechanical work decreases as the speed increases. By comparison, the temperature and force plots indicate very little change in response depending on their level. These results indicate that higher mechanical strengths are achieved with increases in amplitude, decreases in speed, and are not dependent on temperature and force within the levels tested in this study.

As seen in these results, amplitude is the driving and most sensitive variable for bond quality. This result is expected to be from an enhanced scrubbing action which more effectively disperses oxides and contaminants away from the interface, in turn improving the strength of the interface by increasing the density of metallic bonding. This trend cannot necessarily be extrapolated because defects may be introduced within the structure at higher amplitudes; yet this variable appears to have a critical correlation with the mechanical strength of UAM builds within the levels tested.

Speed was also found to have a statistically significant effect on strength. A slower speed allows additional time for scrubbing of the interface and therefore increased ultrasonic energy supplied to the interface for welding. As a result, enhanced dispersion of oxides and contaminants at the interface can be achieved by decreasing the weld speed. Similar to the amplitude observation, it is not known if there is a point of diminishing returns for decreases in speed.

Table 17.4 Optimal weld parameters for Al 6061-H18 as determined by analysis of push-pin tests. The optimization was performed on a Fabrisonic SonicLayer 4000 system; these results do not necessarily apply to other UAM systems

Parameter	Level
Temperature	RT to 93.3°C (200°F)
Force	4000–6000 N
Amplitude	32.8 μm (70%)
Speed	84.6 mm/sec (200 in./min)

Based on this work, optimal weld parameters for Al 6061-H18 foil material in the 9 kW UAM process are presented in [Table 17.4](#).

17.3.2 Process improvements studies

17.3.2.1 Foil overlap and stacking

To create builds wider than 1 in., the UAM process requires abutting foil tapes next to one another, which in turn creates a source for void formation, as shown by Obielodan et al. (2010) [27]. Overlapping of tapes can minimize or prevent void formation at these abutments, but the build surface becomes less uniform due to accumulation of material at the seam locations. This effect is illustrated in [Figure 17.23](#) [44]. Another production factor that must be addressed is the stacking sequence, or stagger, of layers as they progress higher in the build. If the tapes are all aligned at the same location, the possibility of voids running through a single area greatly increases. Therefore moving the seam location in a brick-like fashion to create a less direct crack path, should a crack develop, is ideal. Many methods of stagger can be implemented, but typical patterns use an ordered, or random layup, as shown in [Figure 17.23](#).

UAM builds were constructed to investigate the effect of tape to tape overlap and stacking sequence on strength. Al 6061-H18 foils that were 0.006 in. (0.1524 mm) thick and 1 in. (25.4 mm) wide were used, built onto an Al 6061-T6 baseplate. The weld parameters used for the builds follow previously optimized parameters by Wolcott et al. [9] for Al 6061 presented in [Table 17.4](#). All builds were performed at room temperature using a sonotrode with a roughness of 7 μm R_a .

Two build plates were used to investigate each of the effects with each of the sample sets summarized in [Table 17.5](#). In plate 1, the stacking remained constant, while the tape to tape overlap (α in [Figure 17.23](#)) was varied from 0.0015 in. (0.038 mm) to 0.0045 in. (0.1143 mm). In the SonicLayer system, this is achieved using a constant 1 in. (25.4 mm) wide tape and setting the tape width to varying levels. The specified tape overlaps were selected at levels which provide overlap while minimizing ash, or excess material, at the abutment points. The ordered stacking sequence followed a 0,1,0,-1... pattern as shown in [Figure 17.23](#), with the amount of stagger given by β . In plate 2, the tape overlap was held constant while the stacking sequence was varied. Samples A and B were built using similar 0,1,0,-1,0 ordered stacking sequences with varying amounts of stagger. Build C had random stacking with a maximum stagger value of $\beta = 0.3$ in. (7.62 mm). Build D had ordered stacking with 50% stagger from tape to tape. Stacking sequences were selected such that both randomized and ordered sequences were investigated, and the entire design space of stagger values was covered.

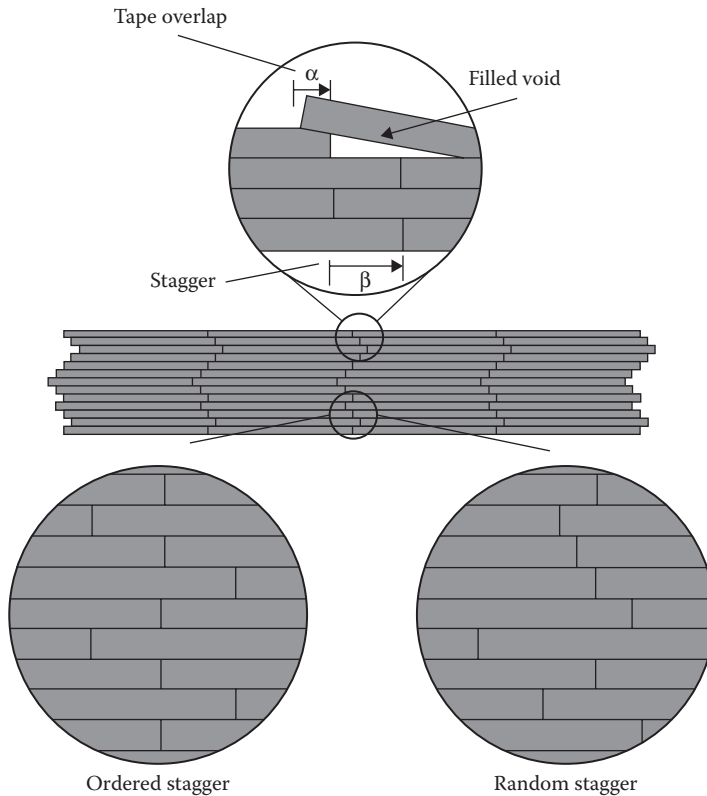


Figure 17.23 Tape overlap and stagger with potential void filled in via plastic deformation of the tape and schematics for ordered and random stagger sequences. (From P. Wolcott, A. Hehr, C. Pawlowski, and M. Dapino, *Journal of Materials Processing Technology*, **233**, 44–52, 2016.)

Table 17.5 Overlap and stacking sequence prescribed for each sample set

Sample set	Overlap (α in in.)	Stacking sequence (β in in.)
1A	0.0015	Ordered with $\beta = 0.15$
1B	0.0025	Ordered with $\beta = 0.15$
1C	0.0035	Ordered with $\beta = 0.15$
1D	0.0045	Ordered with $\beta = 0.15$
2A	0.003	Ordered with $\beta = 0.1$
2B	0.003	Ordered with $\beta = 0.15$
2C	0.003	Random with $\beta = 0.3$ at maximum
2D	0.003	Ordered with $\beta = 0.497$ (50% stagger)

Tensile samples were sectioned from the blocks using the CNC stage on the machine following ASTM subsize tensile sample dimensions [28] such that testing occurred across the various tape interfaces, transverse to the welding direction. Tensile tests were performed on a 22 kip (98.7 kN) Interlaken 3300 test frame, using a displacement rate of 0.05 in./min (1.27 mm/min) while recording the load to failure.

Table 17.6 Ultimate tensile strength results for overlap and stagger study builds

	UTS (MPa)							
	1A	1B	1C	1D	2A	2B	2C	2D
	133.1	121.7	202.3	227.1	225.5	185.1	221.7	184.2
	117.7	129.8	214.7	178.8	177.5	196.3	223.9	163.7
	124	144.2	211.4	228.2	185.1	167.7	222	153.6
Mean	124.9	131.9	209.5	211.4	196	183	222.5	167.2
St Dev	7.7	11.4	6.4	28.2	25.8	14.4	1.2	15.6

The test results are summarized in [Table 17.6](#). From the results of plate 1, there is a clear delineation between the first two samples (A, B) and the last two samples (C, D), with samples C and D producing strengths of approximately 210 MPa on average versus 125 MPa for samples A and B. Results of test data from plate 2 indicate that sample C resulted in the highest tensile strength, 222.5 MPa on average, compared to the other samples.

Based on these results, it is recommended that for UAM block builds, a tape to tape overlap of at least 0.0035 in. (0.0635 mm) should be used and that the stacking sequence follows a random stacking with maximum stagger of 0.3 in. (7.62 mm). The optimal overlap value of at least 0.0035 in. is approximately half the height of the original foil thickness (0.006 in.). This could represent a threshold value whereby the plastic deformation of the foil is able to completely fill the void at the abutting area. Further work using varying thickness foils could be performed to test this hypothesis.

Randomized stacking is shown to produce the highest strength results. It is hypothesized that this is due to the configuration producing a more tortuous crack propagation path. If the abutting points are assumed to be the crack initiation points, failure in the ordered structure would require transmission through only a single layer at a time. In the randomized case, instances of the failure would have to traverse multiple layers, leading to a more complete crack arresting mechanism.

Tape to tape overlap results are consistent with those found by Obielodan et al. [27] in 1 kW UAM, who recommended overlaps of at least 0.00275 in. (0.07 mm). Stacking sequences recommended by Obielodan et al. use a 50% stagger; however, only two stacking methods were investigated, while the study presented here investigated four separate stacking sequences. Of note, these recommendations are based on the testing performed here. A globally optimal value may be achieved through further optimization of these parameters. The recommended stacking sequence proposed is based on the findings from sample 2C, indicating that randomized stacking should be used. However, the magnitude of the proposed stagger may not scale in taller builds where tape flash at the build edge creates areas of poor support leading to inconsistent welds at the build edge. This effect can propagate inward as a build progresses higher, making further welds near the edges difficult. In these instances, a random stacking pattern with smaller stagger should be used.

17.3.2.2 Effects of surface roughness

Periodic flattening passes conducted throughout a build using the CNC stage in state of the art UAM systems can remove excess material at seams due to tape overlap. However, inhomogeneities are created within the build due to the smoothly machined surface following these flattening passes. Consequently, it is necessary to understand how welding onto smooth and textured surfaces affects bond quality.

To study this effect, builds were conducted with welds onto smooth, freshly machined surfaces and welds onto roughened surfaces. Flattening passes were performed using a carbide insert shell mill within the CNC stage of the SonicLayer 4000 UAM machine. Roughened surface samples were built onto surfaces which were textured by vibrating the sonotrode at a low amplitude, similar to weld operations. The roughness of the machined surface was $0.12 \mu\text{m } R_a$, and the roughened surface was $5.7 \mu\text{m } R_a$, measured with a Mitutoyo mechanical probe profilometer. Each build consisted of 20 total layers, such that five flattened surfaces were introduced into each build. All builds were constructed on a 0.5 in. (12.7 mm) thick Al 6061-T6 baseplate with Al 6061-H18 foils 1 in. (25.4 mm) wide and 0.006 in. (0.1524 mm) thick. Sample strength was measured via push-pin testing to compare delamination strength and resistance.

Push-pin test results are provided in [Table 17.7](#); of note, one textured sample was damaged during test setup and was not tested. The mean peak force for the textured samples (4.42 kN) is similar to the nontextured samples (4.45 kN). However, there is a measurable difference in how the two types of samples are measured for mechanical work. The textured samples exhibit an average push-out energy of 5.51 kN-mm compared to 4.75 kN-mm for the nontextured samples, indicating that a larger amount of energy is necessary to produce failure in the textured material.

The improvements in weld properties due to surface texturing are believed to originate at the weld interface. It is hypothesized that the increased surface roughness after texturing enhances asperity deformation during welding leading to increases in plastic deformation, oxide dispersal, mixing, and the driving force for dynamic recrystallization. In combination, these factors increase the potential for grain growth across the bond interface leading to improved metallurgical bonding [11]. To further investigate this phenomenon, in-depth characterization of the grain structure at the interface will be required.

A second study involving surface roughness was performed to determine the effect of sonotrode roughness on weld quality. In this study, samples were fabricated using sonotrodes of $7 \mu\text{m}$ and $14 \mu\text{m } R_a$ roughness, respectively. Both of these sonotrodes were textured with electrical discharge machining to create the desired surface profile. Two 12 in. (30.5 cm) long, 1 in. (25.4 mm) wide build strips, 20 layers tall were constructed using the two different sonotrodes, each with identical weld parameters. The strips were built onto a 0.5 in. thick Al 6061-T6 baseplate, yielding eight total push-pin samples.

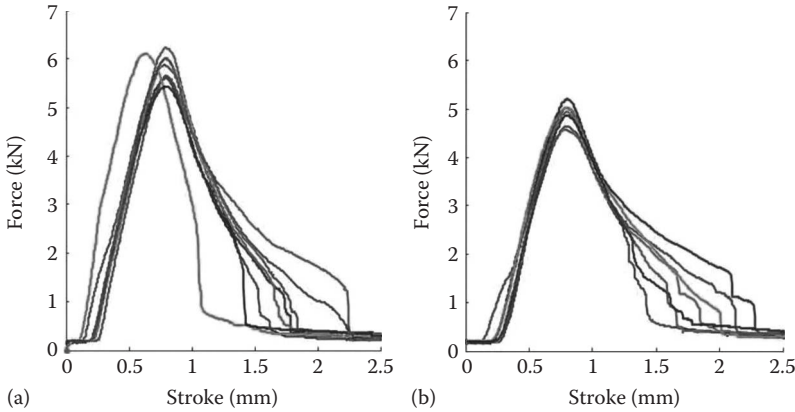
Push-pin results comparing the two sonotrode roughnesses are shown in [Figure 17.24](#) and [Table 17.8](#). As seen in the figure and table, the $14 \mu\text{m}$ samples exhibit a larger peak force until failure and a similar push-out energy compared to the $7 \mu\text{m}$ samples.

Table 17.7 Push-pin data for textured and nontextured builds

Sample	Textured		Nontextured	
	Peak force (kN)	Energy (kN*mm)	Peak force (kN)	Energy (kN*mm)
1	4.66	5.32	4.28	3.82
2	4.18	5.47	4.66	5.50
3	4.42	5.74	4.51	5.58
4	–	–	4.35	4.11
Mean	4.42	5.51	4.45	4.75
St Dev	0.20	0.17	0.15	0.80

Table 17.8 Averaged results of push-pin testing with varying roughness sonotrodes

7 μm Roughness		14 μm Roughness	
Max force (kN)	Energy (kN-mm)	Max force (kN)	Energy (kN-mm)
4.9	7.3	5.8	7.7

**Figure 17.24** Push-pin results: (a) 14 μm R_a and (b) 7 μm R_a .

Based on these measurements, enhanced bond quality can be achieved using a 14 μm R_a roughness sonotrode compared to a 7 μm R_a sonotrode. Li and Soar [29] also noted that rougher sonotrode surfaces produced better bonds when other processing conditions were kept the same. They also reported that rougher surfaces increase the void concentration at weld interfaces. However, interface void presence is essentially nonexistent with 9 kW UAM if appropriate machine settings are used. If this is not the case, for example, for sonotrodes rougher than 14 μm R_a or low weld amplitudes and normal forces, interface voids can still form. Consequently, selecting an optimal surface roughness for a given material or UAM welding application is necessary. Friel et al. [30] discussed this matter as well.

The improved bond quality associated with rougher sonotrodes is likely to originate in the consolidation at the interface, similar to the effect seen in roughened versus smooth surfaces. Due to the creation of larger asperities, more plastic deformation may occur, which would enhance the bonding mechanisms of oxide fracture, dispersal, and increase the driving force for dynamic recrystallization. It is suspected that peak force during push-pin testing is enhanced from the 14 μm sonotrode roughness because it increases the resistance to initial crack formation, whereas push-out energy is largely unaffected because it is a measure of the resistance to crack propagation. Further work using mechanical testing and microscopy is required to understand these failure energy differences.

17.3.2.3 Effect of heat treatments

Heat treatments on UAM components have shown an ability to improve mechanical and microstructural properties [9,31]. Because Al 6061 is a heat-treatable alloy, it is necessary

to determine the strength improvements achievable on postprocessed components. To test the effects of heat treatments on out-of-plane UAM tensile strength, a 0.8 in. (20.32 mm) tall UAM block was fabricated using Al 6061-H18 foils 1 in. (25.4 mm) wide and 0.006 in. (0.1524 mm) thick. This build was constructed using the weld parameters from Wolcott et al. [9] shown in Table 17.4 with a 7 μm horn and no tape to tape overlaps or flattening passes. From this block, nine cylindrical samples were sectioned using wire electrical discharge machining. These samples were sectioned avoiding any seam locations. Three samples were annealed, three were treated to a T6 condition, and three samples were tested as-built. The specific heat treatment temperatures and settings as described by ASM standards are summarized below.

For annealing (O): Heat to 413°C for 2.5 hours, cool at 1°C/min until 280°C, and then air cool [32]. For T6: Heat to 530°C for 1 hr to solutionize, quench in water, and heat to 160°C for 18 hours [32]. H18: indicates an as-built condition. Following heat treatment, samples were machined via CNC lathe to final dimensions for tensile testing. The dimensions for the specimens are based on ASTM standards [28]. Machined specimens were then tested in tension using a 22 kip (98.7 kN) Interlaken 3300 test frame with displacement rate of 0.05 in./min (1.27 mm/min).

Out-of-plane ultimate tensile strength results are summarized in Table 17.9. Comparisons to initial foil stock in each of the H18, T6, and O conditions are presented. H18 comparisons used as-received stock tested in tension with no heat treating, while foils for the annealed and T6 references were processed using the same heat treatment as the samples from the UAM block build. Of note, the elongation values provided are not exact as they represent deflection of the entire load frame measured by the linear variable differential transformer (LVDT). However, the displacement values can provide useful comparative evaluations. Use of an extensometer was not possible due to the small sample size of the specimens. Results show a significant improvement in strength with heat treatment. The T6-treated samples exhibit strength almost 90% of reference material, while annealed samples exhibit strength nearly the same as reference at 97%.

Overall, these results indicate that the mechanical properties of UAM structures can be enhanced considerably when a postprocess heat treatment is applied. This observation coincides well with the microscopy work of others in Al 3003. In particular, Sojiphan et al. [31] observed that the recrystallized grain structure at weld interfaces in optimized aluminum UAM builds was very stable after heat treating. This stable microstructure results in less defects and defect nucleation sites, which in turn improves mechanical properties. It was also observed that significant recrystallization and grain growth occurred in the bulk weld foil after heat treating. Heat treating also enhances precipitate distribution and concentration in Al 6061. Consequently, strength improvements are suspected to be a combination of improved precipitate density and microstructure stability.

Table 17.9 Comparison of UAM tensile strength for various postprocess heat treatments with comparisons to solid material references

Group	Avg. UTS (MPa)	Avg. Elo. (%)	Ref. UTS (MPa)	Ref. Elo. (%)	UTS (%)	Elo. (%)
H18	135.6	1.4	266.1	3.1	51	45
T6	300.3	13.1	337.3	12.5	89	105
O	117.1	13.7	121.1	18.6	97	74

17.3.3 Elastic modulus

Prior research has shown that the failure strength of UAM parts depends on the testing direction with respect to foil orientation due to the presence of interfacial voids [12]. Thus, it is likely that interfacial voids not only have an effect on failure strength, but also have an effect on the elastic properties of UAM components. Therefore, there is a necessity for research focusing on the measurement of the elastic constants in the three material directions (rolling direction, vibration direction, and transverse direction) and the characterization of how interfacial voids affect these elastic constants.

Elastic constants can be measured by mechanical testing. However, due to the small geometries of typical builds and limited yielding, this approach is difficult. Ultrasonic testing can be used as an alternative to mechanical testing for accurate determination of elastic constants [33,34]. The process uses ultrasonic waves which are transmitted and reflected into the sample to measure the elastic constants from speed of sound measurements and measured or estimated material density. Directions and equations for these computations are shown in Figure 17.25.

Foster et al. [33] investigated UAM samples with 65% and 98% bonded areas. The 65% bonded area case was constructed using the 1 kW UAM process, a known procedure for creating joints that contain voids. The 98% bonded area samples were constructed using 9 kW UAM, which significantly limits voids in the weld zone. Step builds were created for each condition, such that accumulative effects could be examined. An example step build is shown in Figure 17.26. Data for the 65% bonded area sample are shown in Table 17.10. The results are presented in comparison to a solid Al 3003 sample with similar measurements taken. A decrease in the elastic moduli is observed for each of the material directions.

Measurements for the 98% bonded area sample are shown in Table 17.11. The elastic constants for this material are significantly closer to solid material than the 65% bonded

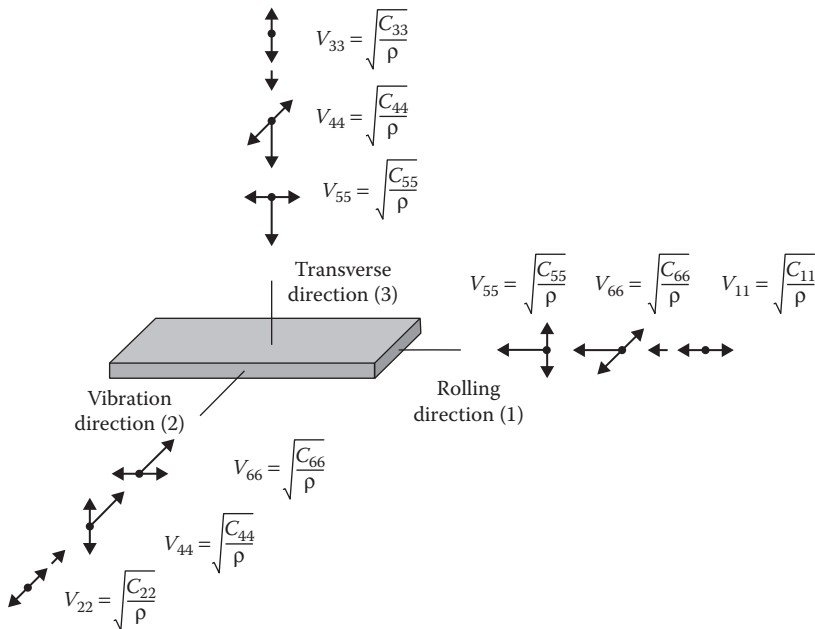


Figure 17.25 Schematic of ultrasonic wave propagation along the three Cartesian directions.

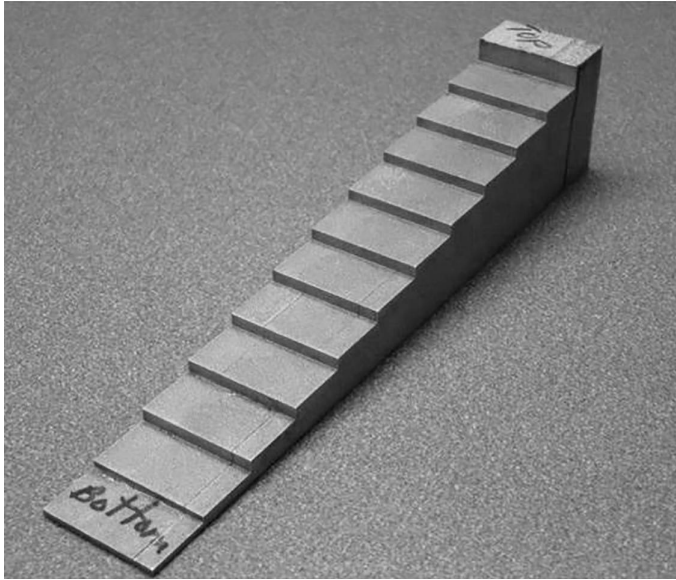


Figure 17.26 Image of step build showing 12 build sections.

Table 17.10 Comparison of elastic constants of 1 kW UAM builds to reference material

	Al 3003-H14 (GPa)	65% Bonded UAM sample	% Difference
C33	108.9	78.2	-28
C44	26.1	23.4	-10
C55	26.1	23.1	-11

Table 17.11 Comparison of elastic constants of 9 kW UAM builds to reference material

	Al 3003-H14 (GPa)	9 kW UAM Al 3003	% Difference
C33	108.7	109.2	0.5
C44	26.1	28.1	7
C55	26.1	28.1	7

area samples. Both the C44 and C55 directions exhibit slightly higher stiffness than the control sample.

It is expected that the lower material stiffness in the 65% bonded sample is due to the presence of voids at the welding interface. These void volumes are filled with no matrix material and thus have negligible mass and strength. As a result, when the material is loaded, the bulk foil portion of the UAM part elastically deforms a small amount, while the interface region under the same load will deform more. This occurs because the load bearing cross-sectional area at the interface is smaller due to the presence of voids for a given load. The combined loading response from the bulk foils and interface region results in an overall greater elastic deformation of the part for a given load. This phenomenon creates a component with an effective stiffness that is lower than the foils used to construct it. The elastic constants measured in samples made by 9 kW UAM were close to those of monolithic aluminum. This is attributed to the low

void content in these samples. Therefore, for components with design requirements for stiffness matching solid material, a voidless bond must be achieved.

17.4 Dissimilar material joining in UAM

17.4.1 Al/Ti dissimilar welding

The low density, high conductivity, and high specific strength and stiffness of Al/Ti composites make them attractive for a number of aerospace, electronic, and automotive applications. Despite these benefits, joining aluminum and titanium can be problematic with conventional methods due to large differences in their melting temperatures, thermal conductivity, coefficient of thermal expansion, and crystal structures. Because UAM operates at low temperatures, much of these issues can be overcome, making it an attractive technology for creating Al/Ti joints.

A study was therefore conducted using 9 kW UAM for joining aluminum and titanium [34]. All welds in this study were performed with a Fabrisonic SonicLayer 4000 9 kW UAM system. Aluminum 1100 foils and commercially pure titanium foils of 0.005 in. (0.127 mm) thick were used. During joining, a bilayer arrangement was used where titanium on top of aluminum was welded in one step, which is shown schematically in Figure 17.27. In this arrangement, the sonotrode is in contact with the titanium layer only. All samples were built onto a solid Al 6061-T6 baseplate with the Al 1100/Al 6061 interface as the first layer. The weld parameters used for the joints are shown in Table 17.12.

Figure 17.28 shows an EBSD scan of an as-built Al/Ti UAM build. Results show significant deformation in the aluminum layers at the titanium–aluminum interfaces. The aluminum layers have a nominal thickness of 127 μm prior to welding, which is reduced to approximately 70 μm after the UAM process. By contrast, the titanium layers are nominally 127 μm prior to welding and 125 μm after welding with layers lower in the build showing more grain refinement and deformation than layers further up the build.

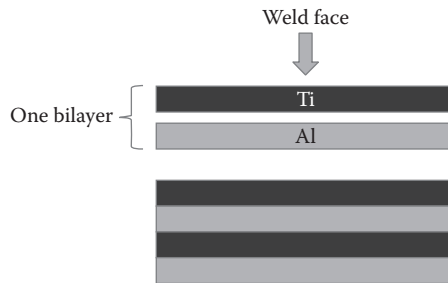


Figure 17.27 Arrangement for Al/Ti bilayers.

Table 17.12 Weld parameters for joining aluminum and titanium

Parameter	Level
Temperature	RT to 93.3°C (200°F)
Force	3500 N
Amplitude	41.55 μm (70%)
Speed	60 in./min (25.4 mm/sec)

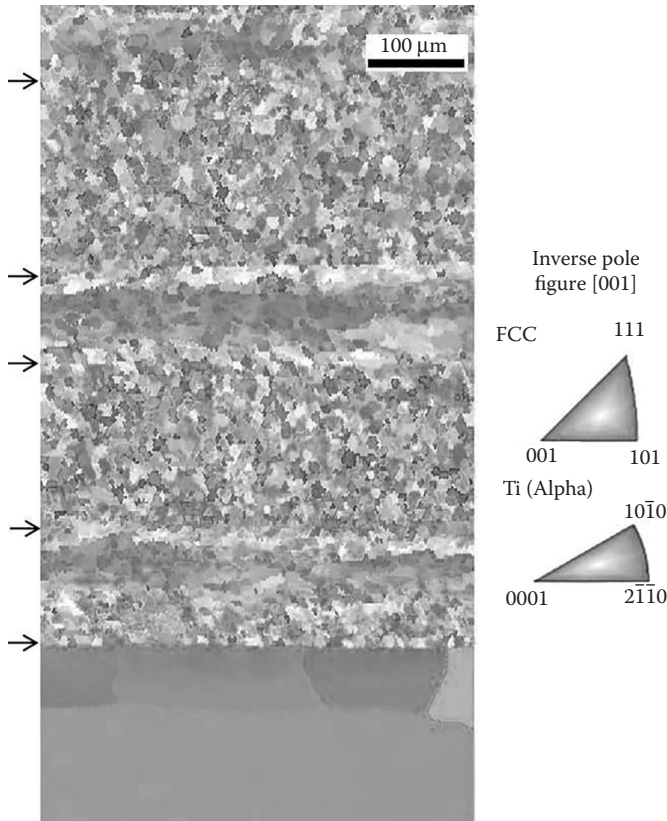


Figure 17.28 Electron backscatter diffraction image of Al/Ti joint. Arrows indicate approximate location of material interfaces.

The microstructure in the titanium layers is unchanged during the welding process, with all deformation and refinement occurring in the softer aluminum layers.

EBSD measurements of an Al/Ti sample heat treated at 600°C for one hour are shown in [Figure 17.29](#). The grain structure in the titanium layers appears unchanged compared to the as-built samples, while the aluminum layers show significant grain growth. In each of the aluminum layers, it appears that the heat treatment has caused preferential grain growth into only a few grains for each layer. Grain growth in the substrate Al 6061 material appears as well, though not to the extent of the growth in Al 1100 layers.

In addition, though not shown in the EBSD results, an intermetallic layer forms at the Al/Ti interfaces. This is an approximately 5 μm thick layer caused by diffusion during the heat treatment process. In addition to microstructural evaluations, mechanical strength was tested via push-pin and shear testing. A summary of the mechanical test results is presented in [Table 17.13](#). The mechanical work, or area under the force-displacement curve, was used as the metric for evaluating the strength of the samples. The heat-treated samples yield much higher values of mechanical work for failure than the as-built samples, roughly 12.7 kN-mm versus 3.5 kN-mm on average. These results indicate that heat treatment significantly increases the mechanical strength of UAM-joined Al/Ti material.

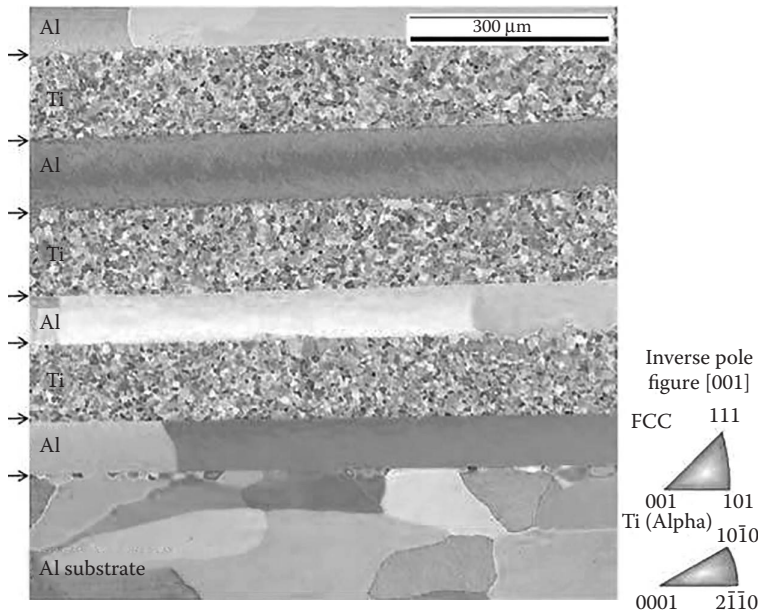


Figure 17.29 Electron backscatter diffraction image of Al/Ti joint after heat treatment. Arrows indicate approximate location of material interfaces.

Table 17.13 Mechanical test results for as-built and heat-treated Al/Ti joints

	Shear strength (MPa)	Pushpin (kN-mm)
As-built	46.3	3.5
Heat-treated	102.4	12.7

Results of shear testing are likewise summarized in [Table 17.13](#) showing the average ultimate shear stress (USS) of the tests. The shear strength of the heat-treated samples exhibits ultimate shear strengths over two times that of the as-built samples with strengths of 102.4 MPa and 46.3 MPa, respectively.

Previous studies have examined various aspects of Al/Ti joining using 1 kW UAM. Using a shear test and 1 kW UAM, Hopkins et al. [19] measured the as-built shear strengths of 63 MPa on average, slightly above the average value of 46.3 MPa for the 9 kW UAM as-built shear strengths measured. Studies by Obielodan et al. [36] using CpTi and Al 3003 suggest the as-built shear strengths of 34 MPa. Following a heat treatment of 480°C for 30 min, shear strengths of 73 MPa were measured while exhibiting diffusion of approximately 5 μm. This diffusion zone was said to provide solid solution strengthening at the interface, not present in the as-built samples. The study presented here demonstrates that shear strengths of 102 MPa on average are possible when using 9 kW UAM and a postprocess heat treatment which generates a similar 5 μm diffusion zone. However, in this case, the diffusion zone is believed to provide a biaxial constraining action at the interface which provides the strengthening. Weld amplitudes of 41.55 μm are expected to increase the plastic deformation at the bond interfaces, thus increasing the driving force for recrystallization at the interface and improving bonding as

compared to the studies using 1 kW UAM. The as-built samples in all three cases lack indications of diffusion which, based on results of heat-treated specimens, is necessary for maximizing mechanical strength.

17.4.2 Steel/Ta joining

Tantalum is an attractive material for corrosive environments and nuclear applications, due to its low permeability to radiative species and high melting temperature [37]. Due to cost, it is advantageous to use tantalum clads whenever possible to take advantage of its material properties without encountering exorbitant costs. Therefore, joints of tantalum and steel are required to meet these goals. However, due to significant differences in melting temperature (Ta: 3020°C and Fe: 1538°C), solid-state welding techniques are preferred over fusion-based welding.

An examination of Ta/Steel welds was conducted using 9 kW UAM [38]. Welds of 99.5% tantalum sheet were joined onto a 1010 steel substrate using the 9 kW UAM process. These joints used a single 50 μm thick tantalum layer as a clad onto a 2.5 mm thick steel substrate. Weld parameters for the joints are shown in Table 17.14. Successful joints were examined using electron microscopy and nanoindentation following joining.

An electron microscopy image of a Ta/Steel joint is shown in Figure 17.30. The image shows three distinct areas that are characteristics of the Ta/Steel joints observed. The first

Table 17.14 Weld parameters for joining tantalum to steel

Parameter	Level
Force	7000 N
Amplitude	36 μm
Speed	35.4 in./min (15 mm/sec)

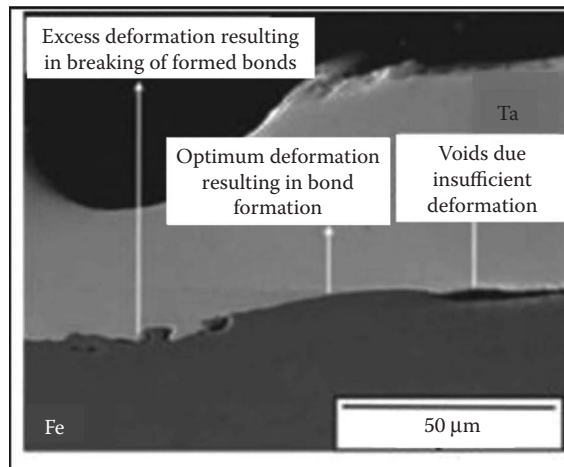


Figure 17.30 Electron microscopy image of Ta/Steel joint showing regions of voids, successful bonding, and areas of excess deformation leading to broken bonds. (From N. Sridharan, M. Norfolk, and S. Babu, *Metallurgical and Materials Transactions A* 47(1), 2517–2518, 2016.)

is a region of voids, where insufficient deformation occurred. Under insufficient deformation, the surface asperities do not collapse, and intimate contact required for bonding does not occur. A second region observed is that of good bonding, characterized by a lack of voids at the interface. The final region observed is excess deformation. In these regions, it is hypothesized that a bond occurs, however continued deformation of the interface leads to breakage of these bonds. This region is characterized by small voids along the interface along with distinct deformation zones that are atypical in the well-bonded areas.

Electron backscatter diffraction results are presented in Figure 17.31 showing the grain map and grain orientation spread (GOS) map at the interface. The interface shows a fine, mostly equiaxed grain structure, while the bulk of the tape suggests little changes to the grain structure. The GOS map in Figure 17.31b shows a gradual increase in the amount of plastic deformation at the interface and into the Ta layer. Within the bond region, the GOS map conveys little plastic deformation indicating that recrystallization has occurred, which is consistent with the equiaxed grain structure found in this region.

This grain structure is similar but not identical to previously measured microstructures for UAM, which indicate dynamic recrystallization at the bond interface [15]. Therefore, a different mechanism must take place to create the microstructural features found in these dissimilar joints featuring body-centered cubic crystal structures. Based on the observed measurements, it is proposed that rotational dynamic recrystallization is occurring. This is a mechanism which has been observed in adiabatic shear bands in Ta alloys where dislocations generated during plastic deformation reach a critical level to form elongated subgrains. These subgrains minimize the strain energy in the lattice, and with continued deformation, eventually break up into equiaxed grains at the interface while continued grain rotation increases the misorientation between grains. This mechanism explains the high-angle grain boundaries observed at the interface. Further deformation would then lead to further refinement and thus the very fine grain structure which is observed.

Nanohardness tests of the tantalum and steel portions of the joint are shown in Figure 17.32. The hardness at the interface is higher than that in the bulk portions of each material. Similarly, the strength decreases for tests further from the interface. Because

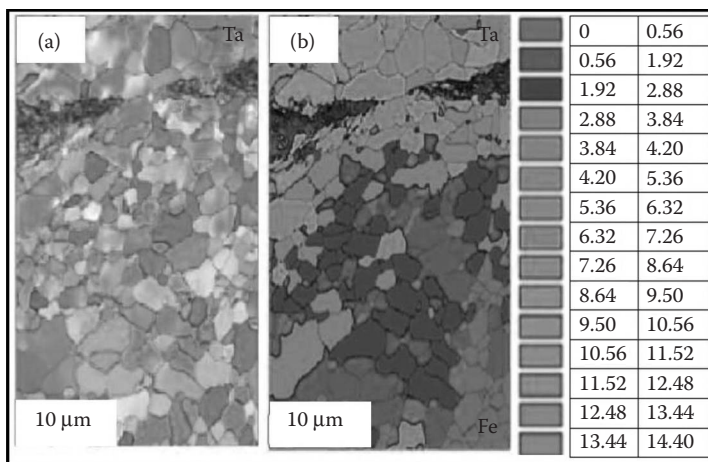


Figure 17.31 Electron backscatter diffraction image of Ta/Steel joint showing (a) grain map and (b) GOS map indicating plastic strain. (From N. Sridharan, M. Norfolk, and S. Babu, *Metallurgical and Materials Transactions A* 47(1), 2517–2518, 2016.)

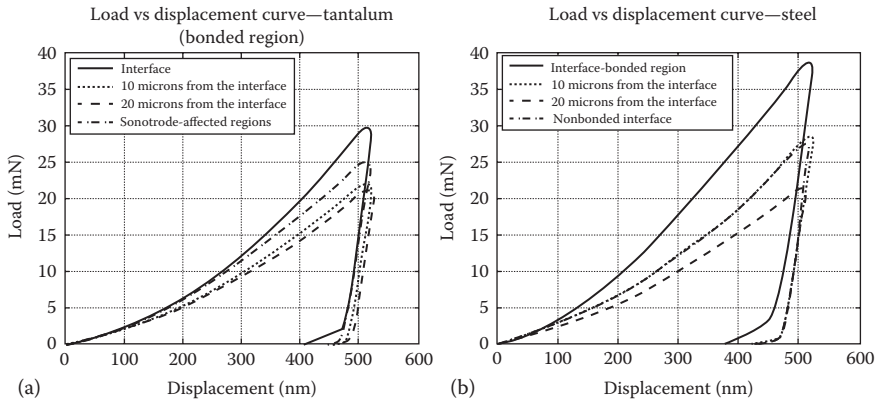


Figure 17.32 Nanohardness testing of (a) tantalum and (b) steel sides of Ta/Steel joint. (From N. Sridharan, M. Norfolk, and S. Babu, *Metallurgical and Materials Transactions A* 47, 1, 2517–2518, 2016.)

higher strength and grain refinement are shown at the interface, it is hypothesized that the strengthening mechanism in this region is due to Hall–Petch strengthening from small grain sizes. Regions close to the interface which show a decrease in hardness are attributed to a decrease in the plastic strain away from the interface. This is generally confirmed in the GOS results, which indicate plastic deformation decreases further from the interface.

17.4.3 Other dissimilar joining

The UAM process is a proven technology for joining a number of other dissimilar material combinations in addition to the Al/Ti and Ta/Steel combinations highlighted. In a study by Truog [25], Al/Cu combinations were proven using the 9 kW UAM process. This work shows that viable Al/Cu welds can be achieved using the UAM process with a cross section from an Al/Cu joint shown in Figure 17.33.

Heat treatments at 350°C for 10 min were shown to significantly improve the bond quality of the joints. Push-pin tests for as-built and heat-treated Al/Cu welds are shown in Figure 17.34. For each welded combination, the joint strength increases following heat treatment. This is consistent with Al/Ti joints which show similar mechanical strength increases following heat treatment, as discussed in Section 17.4.1.

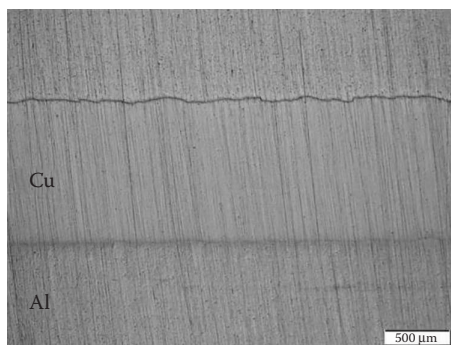


Figure 17.33 Cross section of Al/Cu joint.

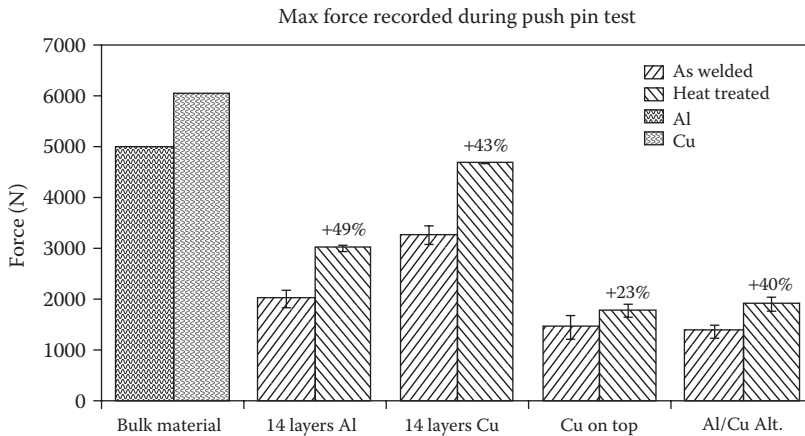


Figure 17.34 Push-pin results for as-welded and heat-treated Al/Cu combinations. (From A. Truog, Bond improvement of al/cu joints created by very high power ultrasonic additive manufacturing, Master's thesis, The Ohio State University, Columbus, OH, 2012.)

Work by Mueller et al. [39] suggests that Al/Cu joints produce very small-scale intermetallic diffusion. Evidence of diffusion is only observable via TEM. This work also confirms the prevailing bond theory for Al/Cu joints based on the concept of dynamic grain recrystallization at the interface through rearrangement of dislocations.

A study by Gonzalez and Stucker [23] proved that stainless steel 316L joints could be achieved using the UAM process. Their work shows that voidless joints can be achieved using the 1 kW UAM process. A cross section of a successful joint is presented in Figure 17.35, where four foils are welded onto an Al 3003 substrate. Following a DOE study, optimal process parameters for the 1 kW UAM process were identified. A normal force of 1800 N, weld rate of 26 in./min, weld amplitude of 27 μm , and baseplate temperature of 400°F were identified as optimal for achieving successful joints.

In a study by Obielodan et al. [20] combinations of titanium, silver, tantalum, aluminum, molybdenum, stainless steel, nickel, copper, and MetPreg (commercial metal matrix composite) were all proven using the UAM process. Figure 17.36 shows a cross section of a joint containing nickel, copper, and silver foils, on an Al 3003 baseplate. Two layers of silver were welded onto the aluminum baseplate, followed by a layer of copper; then a layer of

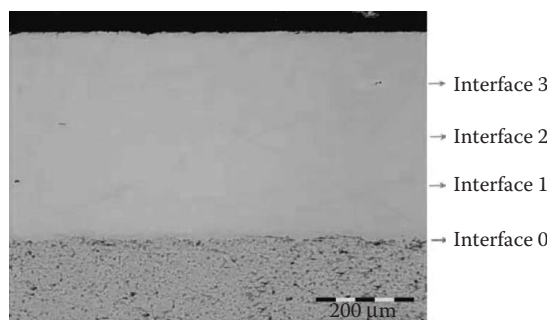


Figure 17.35 Cross section of stainless steel 316L foils welded onto an Al 3003 substrate. (From R. Gonzalez and B. Stucker, *Rapid Prototyping Journal* 18(2), 2012.)

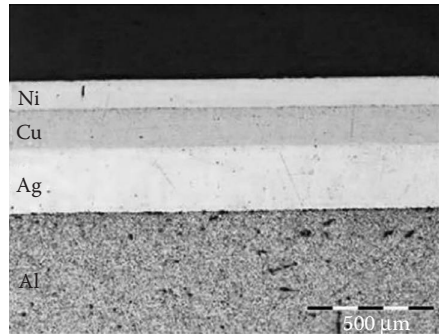


Figure 17.36 Cross section of a multimaterial UAM build including nickel, copper, and silver welded onto an Al 3003 substrate. (From J. Obielodan, A. Ceylan, L. Murr, and B. Stucker, *Rapid Prototyping Journal* 16(3), pp. 180–188, 2010.)

nickel was welded on the top of the structure to complete the build. This build highlights the ability of the UAM process to join multiple material systems.

These works, while not representing all dissimilar material joining using UAM, shows the extent to which the UAM process can be used for joining dissimilar materials. Due to the low process temperatures, dissimilar joints can be achieved for a number of material combinations and encompassing multiple different crystallographic structures.

17.5 Challenges and future directions

A lack of complete scientific understanding of the UAM process and how it affects build properties limits the quality and size of builds as well as the range of dissimilar material combinations that can be additively welded. The underlying challenge is that no comprehensive models exist to describe the UAM process, specifically models which quantify the energy flow in the welder and how the available scrubbing energy effectively induces plastic deformation and dynamic recrystallization in a build. Efforts to model the process have partially addressed this need, but much progress is needed before process–property relationships can be mathematically described and predicted in UAM with any degree of accuracy. The approach to correlate process settings with build properties currently entails DOE studies, though these approaches typically focus on part strength rather than a full set of properties such as strength, fatigue characteristics, functionality, and cost. Examples of existing design of experiment studies were presented in [Section 17.3.1](#).

As is the case with ultrasonic metal welding, the main control variables for the UAM process include weld speed (or time), down force (or pressure), and vibration amplitude [2,8]. Ultrasonic vibration frequency is fixed at the designed resonance frequency of the sonotrode, which is critical for the successful operation of the process. Ringing of the sonotrode at the correct frequency also represents the focus of control strategies implemented within commercial UAM equipment [6].

The input weld energy can be expressed as a function of the main control variables by assuming that weld energy E_{weld} is imparted into a build as mechanical scrubbing,

$$E_{\text{weld}} = \int P \times dt = \int F_s \times \dot{\delta} \times dt = \frac{1}{V_t} \int F_s \times \omega \times \delta \times dx \quad (17.2)$$

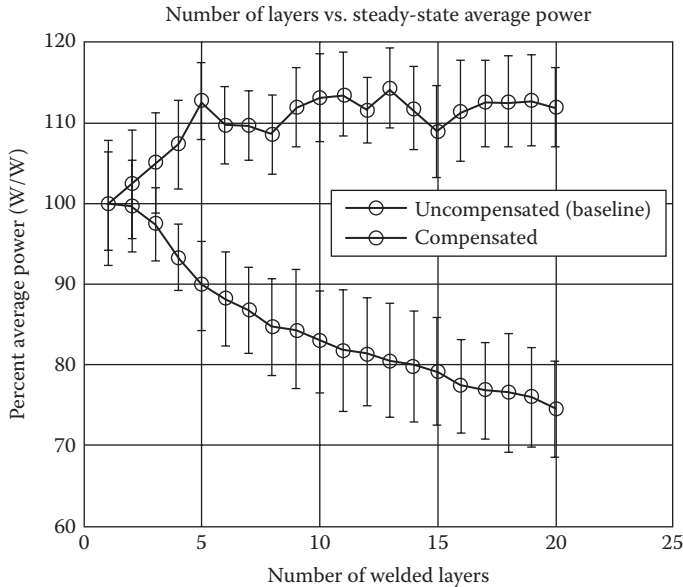


Figure 17.38 Measured power with and without amplitude compensation. The compensated build maintains the power applied to the build within +15%, whereas the uncompensated build shows a decay in input power of 25% by the twentieth layer.

compliance (inverse of stiffness) and a resulting bending motion of the part, the net displacement between the new foil and the rest of the stack is increasingly diminished as part height increases. Since amplitude has been shown to have a significant effect on weld quality, [719,42], this decrease in relative motion will typically lead to a degradation of weld quality through the height of the build.

Measurements presented in [Figure 17.38](#) show that the effective weld power can decrease by as much as 25% after only 20 foils have been welded. Manual compensation of the imparted sonotrode amplitude was shown to effectively prevent a decrease in power. These particular measurements show, in fact, a slight increase in imparted weld energy with build height due to overshoot in the manual compensation. Builds were measured without and with power compensation using push-pin tests. Experimental data are shown in [Figure 17.39](#). The samples built with compensated power exhibit failure through all the welded layers compared to more delamination in the uncompensated samples. Additionally, the compensated samples require additional mechanical work to drive the sample to failure and exhibit slightly higher strength.

Microstructural analysis for the fifth and fifteenth tape interfaces for the uncompensated and compensated power samples is shown in [Figure 17.40](#) with electron microscopy images of ion-etched samples. Interfaces 5 and 15 were chosen for comparison because push-pin testing occurs near layer 5 and above. [Figure 17.40](#) shows fine grains at all the interfaces. However, for the fifteenth uncompensated power weld interface, the recrystallized region is narrow, showing little to no mixing in some areas. On the other hand, the fifteenth compensated power interface shows strong mixing and dimensions similar to the fifth power-compensated interface. The difference in mixing and grain refinement originates from the uncompensated build having received less strain energy than the compensated one.

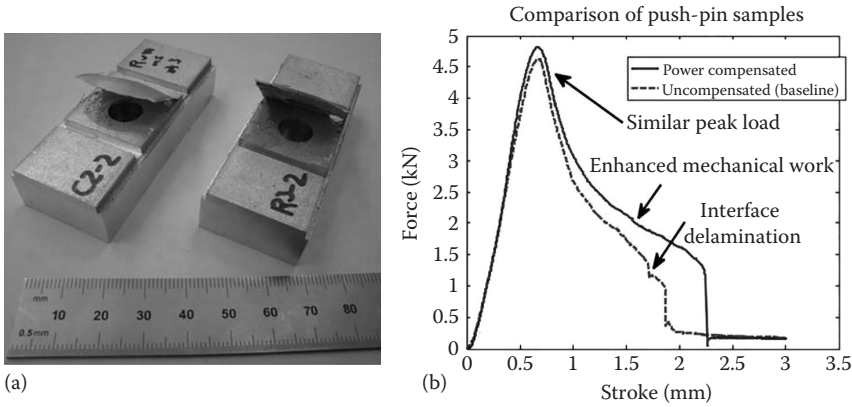


Figure 17.39 Comparison between compensated and uncompensated push-pin samples: (a) photo comparing failure behavior and (b) force-displacement plots.

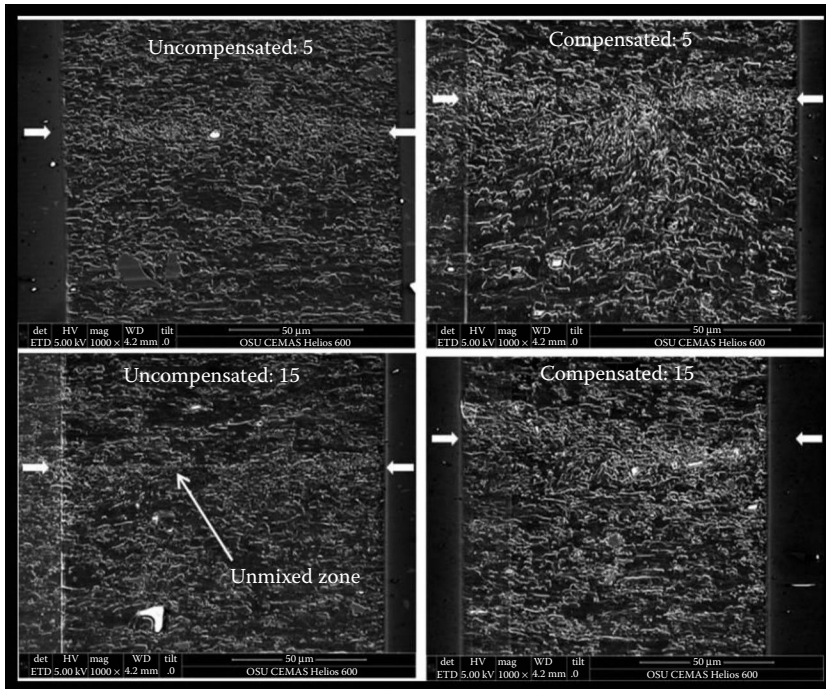


Figure 17.40 SEM image of samples etched with ion beam milling showing interface microstructure at layers 5 and 15 for uncompensated and compensated samples. Arrows indicate the approximate interface region.

The hypothesis of structural compliance impacting ultrasonic weld power and corresponding mechanical strength was tested in this study and found to be influential. It was shown that both mechanical testing and microstructure analysis correlate with variations in weld power input due to poor properties observed when power was not held constant through the UAM process. Consequently, future UAM systems should incorporate means

to monitor and control weld power during the UAM process, rather than operating in amplitude control mode. *In situ* power monitoring and control can be used both to ensure part quality and to monitor any degradation in part quality in real time [41].

The decrease in plastic deformation energy (E_{plastic}) due to compliance can be analyzed by considering the force and displacement involved in plastically deforming the material:

$$E_{\text{plastic}} = F_{\text{plastic}} \int_{\delta_E}^{\delta_{\text{limit}}} d\delta \quad (17.3)$$

where F_{plastic} is the force at which plastic deformation initiates. The integration limits represent the deformation at which elastic deformation ends (δ_E) and the limit prescribed by the controller (δ_{limit}), as shown in Figure 17.37. If one assumes, for simplicity, that the plastic deformation force is constant, the plastic energy can be written in terms of build stiffness (k) as follows:

$$E_{\text{plastic}} = F_{\text{plastic}} \delta_{\text{limit}} - k \delta_E^2 \quad (17.4)$$

This expression shows that the amount of deflection associated with build stiffness, δ_E , has the effect of reducing the available energy to plastically deform the interface. Exact quantification of each of the terms in (Equation 17.4) requires first-principles models which describe the flow of energy through the welder and into the part, including elastic, plastic, and dissipative terms. This requires understanding of the transfer path of input electrical power into mechanical weld power and the energy of a given weld. Using this methodology, a control scheme can be implemented which can account for structural compliance effects during the build process, improving the consistency of welds throughout.

From a process viewpoint, UAM is not compatible yet with mass manufacturing production lines. The existing UAM equipment was designed for small production batches and one-off parts. That being said, because UAM welders can be treated as another tool in a CNC workflow, the potential exists for integration of UAM welders into mass production settings. For instance, a UAM welder can be attached to an end effector for 3D printing or joining of automotive parts in production settings. Given limitations in throughput, these parts may need to be manufactured offline and brought to the assembly line alongside preassembled subsystems. This is a typical approach in automotive manufacturing; so conceptually, UAM could be incorporated into vehicle assembly lines without significant disruption or retooling.

References

1. Wohlers Report, <http://wohlersassociates.com/2013report.htm>, 2013.
2. K.F. Graff, Ultrasonic additive manufacturing, *Welding Fundamentals and Processes*, ASM Handbook, 6A, 2011.
3. P.J. Wolcott, C. Pawlowski, L.M. Headings, and M.J. Dapino, Seam welding of aluminum sheet using ultrasonic additive manufacturing system, *Journal of Manufacturing Science and Engineering*, **139**(1), 011010, 2017.
4. C.Y. Kong, R.C. Soar, and P.M. Dickens, Optimum process parameters for ultrasonic consolidation of 3003 aluminum, *Journal of Materials Processing Technology*, **16**(2), 181–187, 2004.
5. M.R. Sriraman, M. Gonser, H.T. Fujii, S.S. Babu, and M. Bloss, Thermal transients during processing of materials by very high power ultrasonic additive manufacturing, *Journal of Materials Processing Technology*, **211**, 2011.
6. www.fabrisonic.com.

7. C.D. Hopkins, P.J. Wolcott, M.J. Dapino, A.G. Truog, S.S. Babu, and S.A. Fernandez, optimizing ultrasonic additive manufactured Al 3003 properties with statistical modeling, *Journal of Engineering Materials and Technology*, **134**(1), 011004, 2012.
8. K. Graff, J. Devine, J. Keltsos, and N. Zhou, Ultrasonic welding of metals, in *American Welding Society Welding Handbook*, Miami, American Welding Society, 2000.
9. P. Wolcott, A. Hehr, and M.J. Dapino, Optimized welding parameters for Al 6061 ultrasonic additive manufactured composites, *Journal of Materials Research*, **29**(17), 2014.
10. M.R. Sriraman, S.S. Babu, M. Short, Bonding characteristics during very high power ultrasonic additive manufacturing of copper, *Scripta Materialia*, **62**, 560–563, 2010.
11. R. Dehoff, and S.S. Babu, Characterization of interfacial microstructures in 3003 aluminum alloys blocks fabricated by ultrasonic additive manufacturing, *Acta Materialia*, **58**(13), 4305–4315, 2010.
12. D.E. Schick, R.M. Hahnen, R. Dehoff, P. Collins, S.S. Babu, M.J. Dapino and J.C. Lippold, Microstructural characterization of binding interfaces in aluminum 3003 blocks fabricated by ultrasonic additive manufacturing, *Welding Journal*, **89**(5), 105s–115s, 2010.
13. P.J. Wolcott, N. Sridharan, S.S. Babu, A. Miriyev, N. Frage, and M.J. Dapino, Characterisation of Al-Ti dissimilar material joints fabricated using ultrasonic additive manufacturing, *Science and Technology of Welding and Joining*, **21** (2), 114–123, 2016.
14. K. Johnson, *Interlaminar Subgrain Refinement in Ultrasonic Consolidation*. PhD thesis, Loughborough, UK, Loughborough University, 2008.
15. H. Fujii, M. Sriraman, and S. Babu, Quantitative evaluation of bulk and interface microstructures in Al-3003 alloy builds made by very high power ultrasonic additive manufacturing, *Metallurgical and Materials Transactions A*, **42A**, 4045–4055, 2011.
16. E. Mariani and E. Ghassemieh, Microstructure evolution of 6061 O Al alloy during ultrasonic consolidation: An insight from electron backscatter diffraction, *Acta Materialia*, **58**, 2010.
17. S. Shimizu, H. Fujii, Y. Sato, H. Kokawa, M. Sriraman, and S. Babu, Mechanism of weld formation during very-high-power ultrasonic additive manufacturing of Al alloy 6061, *Acta Materialia*, **74**, 2014.
18. L.M. Headings, K. Kotian, and M.J. Dapino, Speed of sound measurement in solids using polyvinylidene fluoride (PVDF) sensors, *Proceedings of ASME Conference on Smart Materials, Adaptive Structures and Intelligent Systems*, SMASIS2013–3206, Snowbird, Utah, September 16–18, 2013.
19. C.D. Hopkins, M.J. Dapino, and S.A. Fernandez, Statistical characterization of ultrasonic additive manufacturing Ti/Al composites, *ASME Journal of Engineering Materials and Technology*, **132**(4), 1–9, 2010.
20. J. Obielodan, A. Ceylan, L. Murr, and B. Stucker, Multi-material bonding in ultrasonic consolidation, *Rapid Prototyping Journal*, **16**(3), 180–188, 2010.
21. I.E. Gunduz, T. Ando, E. Shattuck, P.Y. Wong, and C.C. Dumanidis, Enhanced diffusion and phase transformations during ultrasonic welding of zinc and aluminum, *Scripta Materialia*, **52**, 2005.
22. T.H. Kim, J. Yum, S.J. Hu, J.P. Spicer, and J.A. Abell, Process robustness of single lap ultrasonic welding of thin, dissimilar materials, *CIRP Annals—Manufacturing Technology*, **60**, 2011.
23. R. Gonzalez and B. Stucker, Experimental determination of optimum parameters for stainless steel 316L annealed ultrasonic consolidation, *Rapid Prototyping Journal*, **18**(2), 2012.
24. C. Zhang, A. Deceuster, and L. Li, A method for bond strength evaluation for laminated structures with application to ultrasonic consolidation, *Journal of Materials Engineering and Performance* **18**(8), 1124–1132, 2009.
25. A. Truog, Bond improvement of al/cu joints created by very high power ultrasonic additive manufacturing, Master's thesis, The Ohio State University, Columbus, OH, 2012.
26. A. Dean and D. Voss, *Design and Analysis of Experiments*, Springer, New York, 1999.
27. J. Obielodan, G. J. Ram, B. Stucker, and D. Taggart, Minimizing defects between adjacent foils in ultrasonically consolidated parts, *J. Eng. Mater. Technol* **132**(1), 011006 (Nov 03, 2009)
28. ASTM E8/E8M-16a, *Standard Test Methods for Tension Testing of Metallic Materials*, ASTM International, West Conshohocken, PA, 2016, www.astm.org

29. D. Li and R. Soar, Influence of sonotrode texture on the performance of an ultrasonic consolidation machine and the interfacial bond strength, *Journal of Materials Processing Technology*, **209**, 1627–1634, 2009.
30. R. Friel, K. Johnson, P. Dickens, and R. Harris, The effect of interface topography for ultrasonic consolidation of aluminum, *Materials Science and Engineering A*, **527**, 4474–4483, 2010.
31. K. Sojiphan, S. Babu, X. Yu, and S. Vogel, Quantitative evaluation of crystallographic texture in aluminum alloy builds fabricated by very high power ultrasonic additive manufacturing, in *Solid Freeform Fabrication Symposium*, Austin, TX, 2012.
32. ASM-International, *Heat Treating—Heat Treating of Aluminum Alloys*, Vol. 4, ASM International, 1991.
33. D. Foster, M. Dapino, and S. Babu, Elastic constants of ultrasonic additive manufactured Al 3003-H18, *Ultrasonics*, **53**, 2013.
34. H. Jeong, D. Hsu, R. Shannon, and P. Liaw, Characterization of anisotropic elastic constants of silicon-carbon particulate reinforced aluminum metal matrix composites, part 1, *Metallurgical and Materials Transactions A*, **25A**, pp. 799–809, 1994.
35. P. Wolcott, N. Sridharan, S. Babu, A. Miriyev, N. Frage, and M. Dapino, Characterisation of Al-Ti dissimilar material joints fabricated using ultrasonic additive manufacturing, *Science and Technology of Welding and Joining*, **21**(2), 114–123, 2015.
36. J. Obielodan, B. Stucker, E. Martinez, J. Martinez, D. Hernandez, D. Ramirez, and L. Murr, Optimization of the shear strengths of ultrasonically consolidated Ti/Al 3003 dual-material structures, *Journal of Materials Processing Technology*, **211**, 2011.
37. R. Balliett, M. Coscia, and F. Hunkeler, Niobium and tantalum in materials selection, *Journal of Metals*, **38**(9), 25–27, 1986.
38. N. Sridharan, M. Norfolk, and S. Babu, Characterization of Steel-Ta dissimilar metal builds made using very high power ultrasonic additive manufacturing (VHP-UAM), *Metallurgical and Materials Transactions A*, **47**(1), 2517–2518, 2016.
39. J. Mueller, J. Gillespie, and S. Advani, Effects of interaction volume on x-ray line-scans across an ultrasonically consolidated aluminum/copper interface, *Scanning*, **35**, 2013.
40. A. Hehr and M.J. Dapino, Dynamics of ultrasonic additive manufacturing, *Ultrasonics*, **73**, 49–66, 2017.
41. A. Hehr, P. Wolcott, and M. Dapino, Effect of weld power and build compliance on ultrasonic consolidation, *Rapid Prototyping*, **22**(2), 377–386, 2016.
42. Y. Yang, G. Janaki Ram, and B. Stucker, An experimental determination of optimum processing parameters for Al/SiC metal matrix composites made using ultrasonic consolidation, *Journal of Engineering Materials and Technology*, **129**, 538, 2007.
43. P. Wolcott, A. Hehr, C. Pawlowski, and M. Dapino, Process improvements and characterization of ultrasonic additive manufactured structures, *Journal of Materials Processing Technology*, **233**, 44–52, 2016.
44. G.D. Janaki Ram, C. Robinson, Y. Yang, and B.E. Stucker, Use of ultrasonic consolidation for fabrication of multi-material structures, *Rapid Prototyping Journal*, **13**(4), 226–235, 2007.



Taylor & Francis

Taylor & Francis Group

<http://taylorandfrancis.com>